Water Resources Research®

RESEARCH ARTICLE
10.1029/2023WR036023

Sinuosity-Driven Hyporheic Exchange: Hydrodynamics and Biogeochemical Potentials

Daniel Gonzalez-Duque[1], **Jesus D. Gomez-Velez**[1,2], **Jay P. Zarnetske**[3], **Xingyuan Chen**[4], and **Timothy D. Scheibe**[4]

[1]Department of Civil and Environmental Engineering, Vanderbilt University, Nashville, TN, USA, [2]Environmental Sciences Division, Oak Ridge National Laboratory, Climate Change Science Institute, Oak Ridge, TN, USA, [3]Department of Earth and Environmental Sciences, Michigan State University, East Lansing, MI, USA, [4]Pacific Northwest National Laboratory, Richland, WA, USA

Key Points:

- We assess the role of hydrodynamic drivers and modulators in the hyporheic exchange and the biogeochemical potential of meandering rivers
- The meander neck in high-sinuosity channels shields the effect of regional groundwater fluxes, resulting in persistent hyporheic zones
- Hyporheic denitrification potential decreases with increasing sinuosity, and dissolved and particulate organic carbon availability limits it

Supporting Information:

Supporting Information may be found in the online version of this article.

Correspondence to:

D. Gonzalez-Duque and J. D. Gomez-Velez,
daniel.gonzalez@vanderbilt.edu;
gomezvelezjd@ornl.gov

Citation:

Gonzalez-Duque, D., Gomez-Velez, J. D., Zarnetske, J. P., Chen, X., & Scheibe, T. D. (2024). Sinuosity-driven hyporheic exchange: Hydrodynamics and biogeochemical potential. *Water Resources Research*, *60*, e2023WR036023. https://doi.org/10.1029/2023WR036023

Received 4 AUG 2023
Accepted 9 FEB 2024

Author Contributions:

Conceptualization: Daniel Gonzalez-Duque, Jesus D. Gomez-Velez, Jay P. Zarnetske, Xingyuan Chen, Timothy D. Scheibe
Data curation: Daniel Gonzalez-Duque, Jesus D. Gomez-Velez
Formal analysis: Daniel Gonzalez-Duque, Jesus D. Gomez-Velez

© 2024 Oak Ridge National Laboratory, managed by UT–Battelle, LLC, Battelle Memorial Institute and The Authors.
This is an open access article under the terms of the Creative Commons Attribution-NonCommercial-NoDerivs License, which permits use and distribution in any medium, provided the original work is properly cited, the use is non-commercial and no modifications or adaptations are made.

Abstract

Hydrologic exchange processes are critical for ecosystem services along river corridors. Meandering contributes to this exchange by driving channel water, solutes, and energy through the surrounding alluvium, a process called sinuosity-driven hyporheic exchange. This exchange is embedded within and modulated by the regional groundwater flow (RGF), which compresses the hyporheic zone and potentially diminishes its overall impact. Quantifying the role of sinuosity-driven hyporheic exchange at the reach-to-watershed scale requires a mechanistic understanding of the interplay between drivers (meander planform) and modulators (RGF) and its implications for biogeochemical transformations. Here, we use a 2D, vertically integrated numerical model for flow, transport, and reaction to analyze sinuosity-driven hyporheic exchange systematically. Using this model, we propose a dimensionless framework to explore the role of meander planform and RGF in hydrodynamics and how they constrain nitrogen cycling. Our results highlight the importance of meander topology for water flow and age. We demonstrate how the meander neck induces a shielding effect that protects the hyporheic zone against RGF, imposing a physical constraint on biogeochemical transformations. Furthermore, we explore the conditions when a meander acts as a net nitrogen source or sink. This transition in the net biogeochemical potential is described by a handful of dimensionless physical and biogeochemical parameters that can be measured or constrained from literature and remote sensing. This work provides a new physically based model that quantifies sinuosity-driven hyporheic exchange and biogeochemical reactions, a critical step toward their representation in water quality models and the design and assessment of river restoration strategies.

Plain Language Summary

Meandering causes pressure gradients that induce water flow from the channel to the alluvial aquifer and back to the channel. This circulation process is known as sinuosity-driven hyporheic exchange, and it has traditionally been associated with ubiquitous and favorable impacts on ecosystem services. However, its presence and biogeochemical implications can vary across river networks and even result in detrimental conditions. Here, we conducted a systematic modeling study to understand the hydrodynamics of sinuosity-driven hyporheic exchange and its implications for nitrogen transformations. Our results show that the compressing effect of RGF can significantly reduce or vanish the hyporheic zone. Yet, narrow meander necks, characteristic of high-sinuosity channels, shield the hyporheic zone even under extreme regional gradients. This shielding effect has been previously ignored and highlights the persistent nature of the exchange and its resilience against external modulators. We also use our model to propose and evaluate a framework based on measurable physical and biogeochemical parameters to identify the conditions leading to a meander acting as a net source or sink of nitrogen. These mechanistic insights can guide the design and evaluation of river restoration strategies and provide a critical foundation for its representation in water quality models.

1. Introduction

Connectivity along river corridors plays a critical role in ecosystem services (Harvey & Gooseff, 2015; Harvey & Schmadel, 2021; Harvey et al., 2018). For example, it provides thermal (Arrigoni et al., 2008; Holmes, 2000; White et al., 1987; Wu et al., 2020, 2021) and nutrient regulation (Bencala, 2011; Harvey et al., 2018; Holmes, 2000) for streams and rivers. Connectivity encompasses exchange processes that move water, energy, and solutes between rivers and their surrounding surface and subsurface waters (Pringle, 2001), increasing the

Funding acquisition: Jesus D. Gomez-Velez
Investigation: Daniel Gonzalez-Duque, Jesus D. Gomez-Velez
Methodology: Daniel Gonzalez-Duque, Jesus D. Gomez-Velez
Project administration: Jesus D. Gomez-Velez
Resources: Daniel Gonzalez-Duque, Jesus D. Gomez-Velez
Software: Daniel Gonzalez-Duque, Jesus D. Gomez-Velez
Supervision: Jesus D. Gomez-Velez
Validation: Daniel Gonzalez-Duque, Jesus D. Gomez-Velez
Visualization: Daniel Gonzalez-Duque, Jesus D. Gomez-Velez
Writing – original draft: Daniel Gonzalez-Duque, Jesus D. Gomez-Velez
Writing – review & editing: Daniel Gonzalez-Duque, Jesus D. Gomez-Velez, Jay P. Zarnetske, Xingyuan Chen, Timothy D. Scheibe

contact time with reactive environments and enhancing the biogeochemical processes supporting aquatic life (Dent et al., 2000, 2001; Pringle, 2003). Modeling these exchange processes in rivers at the local and catchment scales can provide useful tools for water management and remedial strategies (Arora et al., 2022; Hancock, 2002; Harvey & Gooseff, 2015; Krause et al., 2022; Lewandowski et al., 2019; Ward & Packman, 2019).

Hyporheic exchange is one connectivity process of particular interest as it circulates water, solutes, and energy through reactive environments, serving as a natural biogeochemical reactor modulating water quality across the river network (Boano et al., 2014). This exchange process occurs vertically and laterally and is driven by spatial variations in the hydraulic head (both the hydrodynamic and hydrostatic components) at the sediment-water interface, resulting in the circulation of water and the constituents it carries through the floodplain sediments before returning to the channel (Boano et al., 2014; Tonina & Buffington, 2009). The mechanisms that drive hyporheic exchange are dictated by river geomorphological features at various scales, influencing the direction, magnitude, and stability of the hyporheic flow (Buffington & Tonina, 2009; Poole et al., 2006) and controlling the residence times and biogeochemical processes (Buffington & Tonina, 2009). Previous efforts have proposed methodologies to quantify the relative role of different geomorphic features in the overall channel hyporheic exchange (e.g., Buffington et al., 2004; Gomez-Velez et al., 2015; Harvey et al., 2018; Kiel & Bayani Cardenas, 2014). These methodologies suggest that even though both vertical and lateral exchange processes persist across river networks, vertical exchange plays a dominant role given the fragility of sinuosity-driven exchange to regional groundwater flow (RGF) (Gomez-Velez et al., 2015). However, as shown in this study, sinuosity-driven exchange may be more resilient than previously thought due to the hydrodynamic shielding caused by the neck of high-sinuosity channels (more details in Section 3.1).

Meanders are one of the ubiquitous geomorphic features driving channel water, solutes, and energy through the surrounding alluvium, a process called sinuosity-driven hyporheic exchange. Their planimetry is characterized by multiscale (Lazarus & Constantine, 2013; Leopold & Wolman, 1960; Seminara, 2006; Vermeulen et al., 2016) and self-similar (Montgomery, 1996; Snow, 1989) patterns, which further influence the nature of the exchange process. In fact, throughout river networks, from headwaters to coasts, similar topologies (i.e., shapes) can be found in channels of all sizes. Even though the meander geometry (i.e., length scales) differs drastically between small streams and large rivers, we can find similar meandering patterns at both scales (Anderson & Anderson, 2010; Leopold & Wolman, 1960). This topological commonality is fundamental to proposing a transferable understanding of sinuosity-driven hyporheic exchange.

Numerous studies have explored the underlying mechanisms and hydrodynamic effects behind the sinuosity-driven hyporheic exchange, addressing the importance of channel sinuosity in driving and regulating the hyporheic flow and its residence times (see review by Boano et al., 2014). Channel curvature produces hydraulic gradients between the channel and the alluvium that drive exchange and control the residence time of water (Boano et al., 2006; Cardenas, 2008; Peterson & Sickbert, 2006). For example, meanders with high sinuosity (i.e., sinuosities larger than approximately 2.5, typically characterized by a well-defined meander neck) produce low-velocity zones near the meander apex, allowing for longer contact times with the reactive environment (Boano, Demaria, et al., 2010; Cardenas, 2008; Revelli et al., 2008). As meanders evolve, their planimetry elongates and closes, creating a neck in the base of the meander. This is a common feature of natural meanders that results in strong hydraulic gradients over the narrowest parts of the meander (Boano et al., 2006; Peterson & Sickbert, 2006), inducing faster hyporheic flow along the neck and, therefore, shorter residence times with important implications for biogeochemical transformations (Boano, Demaria, et al., 2010; Revelli et al., 2008). A previous study for low-sinuosity meanders (i.e., sinuosities lower than approximately 2.5, idealized as sinusoidal shapes that cannot capture the formation of meander neck) has shown the tight connection between hyporheic exchange residence time distributions and sinuosity, valley slope, aquifer dispersity, and hydraulic conductivity (Gomez et al., 2012). This analysis was later extended to account for the dynamics induced by river stage fluctuations (Gomez-Velez et al., 2017) and evaporation from riparian vegetation (Kruegler et al., 2020).

Sinuosity-driven hyporheic exchange is embedded within and modulated by the RGF, which compresses the hyporheic zone and potentially diminishes its overall impact. This modulating effect has been explored by Cardenas (2009b), where low-sinuosity meanders were exposed to varying degrees of RGF under gaining and losing conditions. His study focused on the net amount of exchange and the extent of the hyporheic zone, which are highly sensitive to RGF, with relatively small fluxes significantly compressing and, sometimes, obliterating the hyporheic zone. This high sensitivity to RGF is reflected in the cumulative effects of this exchange process at

19447973, 2024, 4, Downloaded from https://agupubs.onlinelibrary.wiley.com/doi/10.1029/2023WR036023, Wiley Online Library on [03/07/2024]. See the Terms and Conditions (https://onlinelibrary.wiley.com/terms-and-conditions) on Wiley Online Library for rules of use; OA articles are governed by the applicable Creative Commons License

19447973, 2024, 4, Downloaded from https://agupubs.onlinelibrary.wiley.com/doi/10.1029/2023WR036023, Wiley Online Library on [03/07/2024]. See the Terms and Conditions (https://onlinelibrary.wiley.com/terms-and-conditions) on Wiley Online Library for rules of use; OA articles are governed by the applicable Creative Commons License

the catchment scale (Gomez-Velez & Harvey, 2014; Gomez-Velez et al., 2015; Kiel & Bayani Cardenas, 2014). However, these previous studies assessing the impacts of RGF do not explore the hydrodynamic effects of complex river planimetry on the compression of the hyporheic zone. As we show in this study, the strong hydraulic gradients induced by the meander neck can counteract the effects of regional groundwater gradients, resulting in a persistent sinuosity-driven hyporheic zone with implications for connectivity and water quality more important than we ever thought.

Although residence times are a critical indicator of biogeochemical reactions, this metric is not the only factor involved in the reaction processes. Reactivity strongly depends on the relative magnitude of the hyporheic transport time scale, the hyporheic zone reaction rates (Gu et al., 2007; Zarnetske et al., 2012), and the availability of chemical constituents involved in the reaction of interest (Sawyer, 2015). From the perspective of nitrogen cycling and the role of hyporheic exchange in nutrient retention, a process that is critical for water quality, as it limits or enhances the chemical transformations (Harvey et al., 2018), these constraints have been studied in detail (e.g., Boano, Demaria, et al., 2010; Gu et al., 2007; Zarnetske et al., 2011a). For example, the works of Gu et al. (2007) and Zarnetske et al. (2012) used a one-dimensional modeling framework to show how increasing values of the aerobic respiration Damköhler number, Da_O (ratio between the characteristic times of reaction and transport), enhance the removal of nitrates in the hyporheic zone of streambeds. Furthermore, nitrogen cycling is also limited by the availability of dissolved organic carbon (DOC) and ammonia (NH_4^+) (Zarnetske et al., 2011a, 2012), where the removal of nitrates (NO_3^-) is associated with the presence of DOC in the hyporheic zone either transported from the stream or locally dissolved from POC (e.g., Sawyer, 2015; Stelzer et al., 2015; Zarnetske et al., 2011b).

Quantifying the role of sinuosity-driven hyporheic exchange at the reach-to-watershed scale requires a mechanistic understanding of the interplay between drivers (e.g., meander planform) and landscape modulators (e.g., RGF) and its implications for biogeochemical transformations. This issue remains a gap in our knowledge, and this study aims to provide new insight from the perspective of flow hydrodynamics and the transformation of nitrogen with the sinuosity-driven hyporheic zone, allowing the systematic comparison to multiple scales of meanders in the river network. We propose a dimensionless framework to systematically explore hyporheic flow and residence times under different sinuosities and regional groundwater gradients while including the effects of reaction time scales and the availability of chemical constituents. In particular, this study builds on the work of Gomez-Velez et al. (2017) by representing more complex channel planimetries that span the full spectrum of meanders observed in nature, describing the age distribution, not only its mean and explicitly modeling nitrogen transformations to estimate the hyporheic zone's biogeochemical potential.

2. Methods

We use a reduced-complexity model to explore sinuosity-driven hyporheic exchange's hydrodynamics, transport, and biogeochemical potential. Our approach explicitly represents the effects of (a) planform (meandering pattern), (b) channel hydraulics, (c) alluvium's physical and biogeochemical properties, and (d) the modulating effect of RGF. We used COMSOL Multiphysics (COMSOL AB, 2024), a finite-element code for all simulations. We generated free-triangular meshes for the four meander geometries with significant refinement near the boundaries and within the meander. In all cases, the mesh quality was high (with a skewness average element quality of 0.90 (Gothäll, 2022)), and the simulations were mesh-independent.

2.1. Reduced-Complexity Model

The physical and biogeochemical process controlling sinuosity-driven hyporheic exchange and its biogeochemical potential in natural systems is highly complex (e.g., Dwivedi et al., 2018); however, in the spirit of Vušanović and Voller (2021), we use a reduced-complexity model, where only the first-order controls for flow and transport are represented. The assumption is that this simplification of the underlying mechanisms captures the general exchange patterns within the alluvium without compromising the predictive outcomes of the physical processes and highlights general and generalizable trends in the system's response. Our conceptualization mimics an alluvial valley characterized by a meandering river that fully penetrates the alluvial valley aquifer, which overlies an older, horizontal, low-permeability river deposit (Figures 1c and 1d). The channel (boundary $\partial\Omega_c$ in Figure 1c) is described by a Kinoshita curve (Abad & Garcia, 2009; Kinoshita & Miwa, 1974; Seminara, 2006; Seminara et al., 2001), which is expressed as a parametric curve:

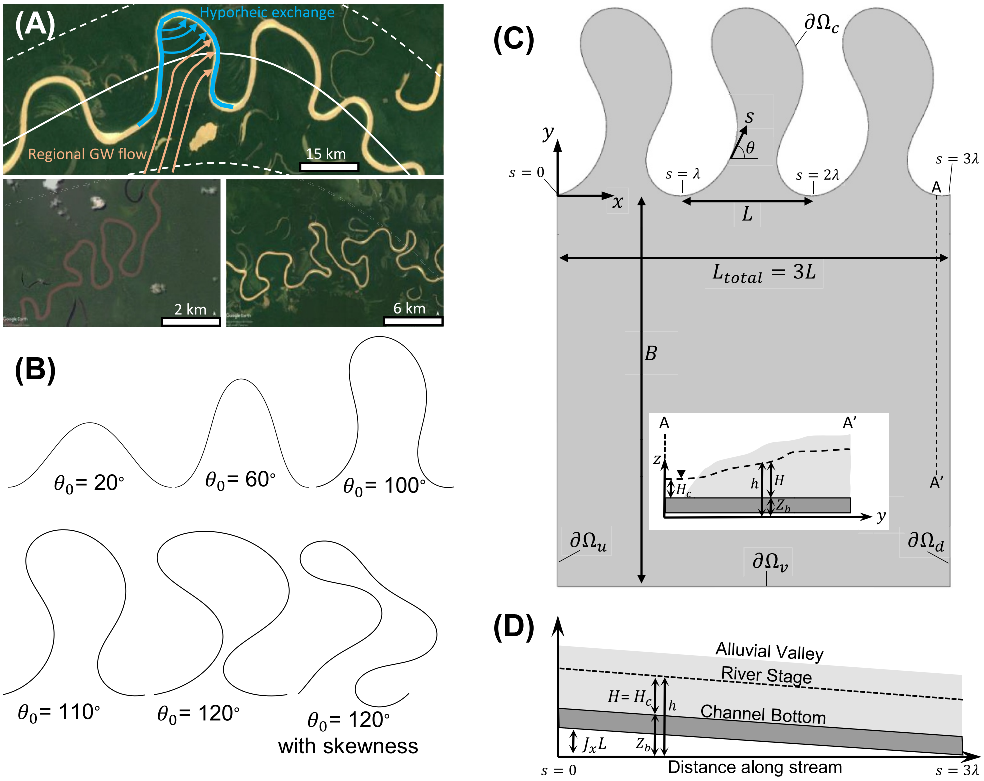

Figure 1. *Conceptualization of the reduced-complexity model for sinuosity-driven hyporheic exchange*. (a) Examples of meandering channels at different scales (images taken from Google Earth). The river in the upper image illustrates the alluvial valley axis (solid black line), the alluvial belt (dashed black line), and the flow field of a single meander bend dictated by the interaction of sinuosity-driven hyporheic exchange (cyan arrows) and regional groundwater flow (orange arrows). (b) Examples of meanders generated with a Kinoshita curve for different values of the maximum angular amplitude θ_0. In these synthetic meanders, the wavelength ($\lambda = 100$), flatness coefficient ($J_f = 1/192$), and skewness coefficient ($J_s = 1/32$) are constant, except for the last meander where $J_s = 1/10$. Planimetric view (c) and longitudinal view along the channel (d) of the domain used in the model. The model focuses on a single meander bend described by a Kinoshita curve ($\partial\Omega_c$). To minimize boundary effects, we repeat this meander unit three times and assume periodic boundary conditions for flow and transport in the downstream ($\partial\Omega_d$) and upstream ($\partial\Omega_u$) boundaries. Our analyses focus on the meander bend in the middle of the domain. The alluvial valley length is $B = 3\lambda$, which is selected to minimize numerical artifacts in the simulated hyporheic flow field caused by the influence of the valley-side boundary ($\partial\Omega_v$).

$$\theta(s) = \theta_0 \sin\left(\frac{2\pi}{\lambda}s\right) + \theta_0^3\left[J_s \cos\left(\frac{6\pi}{\lambda}s\right) - J_f \sin\left(\frac{6\pi}{\lambda}s\right)\right], \tag{1}$$

where θ is the angle between the channel centerline and the down-valley direction [–], s is the streamwise coordinate [L], θ_0 is the maximum angular amplitude [–], λ is the arc wavelength [L], J_s is the skewness coefficient [–] and J_f is the flatness coefficient [–]. Given these parameters, we can calculate the length of the meander bend in the direction of the alluvial axis L [L] and estimate the sinuosity for an individual meander as $\sigma = \lambda/L$.

The Kinoshita curve's flexibility and simplicity make it ideal for exploring the similarities in meander planform across scales in river networks. This curve is flexible enough to reproduce the main planimetric features of individual meanders, including "flattening" and "skewing" of meander loops (Camporeale et al., 2007). For example, compare the meanders in Figure 1a with the curves in Figure 1b. Also, the curve only requires three parameters (θ_0, J_s, and J_f), with the arc wavelength λ serving as a scaling factor. As we show in the following sections, this is a major advantage to nondimensionalize the model, reducing the computational burden and generalizing our results.

We focus our analysis on the flow, transport, and reactivity of sinuosity-driven hyporheic exchange in a single meander bend; however, our numerical implementation uses a periodic modeling domain with three meanders to

19447973, 2024, 4, Downloaded from https://agupubs.onlinelibrary.wiley.com/doi/10.1029/2023WR036023, Wiley Online Library on [03/07/2024]. See the Terms and Conditions (https://onlinelibrary.wiley.com/terms-and-conditions) on Wiley Online Library for rules of use; OA articles are governed by the applicable Creative Commons License

minimize boundary effects. The total length of the modeling domain in the direction of the alluvial axis (x) is $3L$. Boundary conditions for flow and transport processes along the downstream ($\partial\Omega_d$) and upstream ($\partial\Omega_u$) boundaries are assumed periodic to mimic an infinite domain. More specifically, for water flow, we maintain a constant hydraulic head drop, given by the slope of the channel, along these boundaries (the sensitivity analysis for the periodic heads is presented in Text S1 and Figure S1 in Supporting Information S1). For transport, we mirror concentrations along these boundaries. The boundary within the alluvial valley belt ($\partial\Omega_v$) is located at a distance $B = nL$ from the channel. Based on a sensitivity analysis (presented in Text S1 and Figure S2 in Supporting Information S1), the factor $n = 1$ was selected to minimize the influence of the alluvial belt boundary on the flow field.

In the following subsection, we describe the physics and mathematical conceptualization used to describe water flow, the evolution of the water age, and the fate and transport of key constituents involved in the denitrification process (nitrate, ammonium, oxygen, and DOC).

2.1.1. Flow Model

We model a two-dimensional homogeneous and isotropic alluvial aquifer bounded by a fully penetrating channel (Figures 1c and 1d). This assumption is fundamental for the Dupuit-Forchheimer approximation (predominantly horizontal flow) (Troch et al., 2013) and has been used in previous studies focusing on lateral sinuosity-driven hyporheic exchange (Boano, Camporeale, & Revelli, 2010; Boano et al., 2006; Cardenas, 2009a, 2009b; Gomez et al., 2012; Gomez-Velez et al., 2017). Although this assumption neglects the vertical flow induced by partially penetrating channel (e.g., Boano, Camporeale, & Revelli, 2010), it is a reasonable approximation given the scale of the analysis and the focus on lateral circulation cells. With the latter in mind, we use the following continuity equation to describe the spatial distribution of hydraulic head ($h(\mathbf{x})$; [L]) under steady-state conditions (Bear, 1972; Bear & Cheng, 2010):

$$\nabla \cdot \mathbf{Q} = 0, \tag{2}$$

where $\mathbf{Q}(\mathbf{x}) = -KH\nabla h$ is the vertically integrated flux [$\mathrm{L}^2\mathrm{T}^{-1}$], $\mathbf{q}(\mathbf{x}) = \mathbf{Q}(\mathbf{x})/H = -K\nabla h$ is the Darcy flux [LT^{-1}], $\mathbf{x} = [x, y]$ is the spatial coordinate vector [L], K is the hydraulic conductivity [LT^{-1}], $H(\mathbf{x}) = h - Z_b$ is the saturated thickness [L], and $Z_b(x)$ is the vertical location of the impermeable layer elevation with respect to a reference datum $z = 0$ [L]. See Figure 1c and inset for the cross-section A-A′ for additional details. For simplicity, and without loss of generality, we assume $Z_b(x) = J_x(3L - x)$, with J_x [–] and L [L] the average valley slope and the meander wavelength in the direction parallel to the alluvial valley axis (x-direction), respectively.

Boundary conditions are imposed to resemble a periodic system of meander bends running along the alluvial valley axis. The hydraulic head along the meandering channel ($\mathbf{x} \in \partial\Omega_c$) is given by $h(\mathbf{x}) = H_c + (3L)J_x - \frac{J_x}{\sigma}s(\mathbf{x})$, where $\sigma = \lambda/L$ is the meander sinuosity [–], $s(\mathbf{x})$ is the arc length along the channel [L], and H_c is the channel saturated thickness [L]. The model is minimally affected by changes in H_c; therefore, we assumed a typical value of 10 m characteristic of alluvial aquifers (Larkin & Sharp, 1992). A periodic boundary condition is assumed for the lateral boundaries ($\mathbf{x} \in \partial\Omega_u \vee \partial\Omega_d$), where a prescribed hydraulic head drop proportional to the average valley slope is imposed, resulting in $h(x = 3L, y) = h(x = 0, y) - (3L)J_x$. Finally, we assume that flow along the alluvial valley boundary ($\mathbf{x} \in \partial\Omega_v$) is given by $\mathbf{n} \cdot \mathbf{Q} = -KHJ_y$, with J_y [–] the average slope of the far-field water table perpendicular to the alluvial valley axis (y-direction) and $\mathbf{n}$ an outward unit vector. In this case, we use J_y to capture the role of RGF under neutral ($J_y = 0$), gaining ($J_y > 0$), or losing ($J_y < 0$) conditions.

To aid the interpretation and parameterization of scenarios, we recast the flow model in nondimensional terms. This is also done for all the processes that we model and is described in detail in Supporting Information S1. After nondimensionalization, the solution to this problem for the dimensionless hydraulic head ($h^* = h/(J_x\lambda)$), vertically integrated flux $\left(\mathbf{Q}^* = \mathbf{Q}/Q_c = \mathbf{Q}/\left(KJ_x^2\lambda\right)\right)$, Darcy flux ($\mathbf{q}^* = \mathbf{q}/q_c = \mathbf{q}/(KJ_x)$), or any boundary-integrated flux metric only depends on the following dimensionless variables (see Text S2 in Supporting Information S1 for a detailed derivation):

$$\sigma = \sigma\left(\theta_0, J_f, J_s\right), \quad \Pi_{H_c} = \frac{H_c}{J_x\lambda} \quad \Pi_{J_y} = \frac{J_y}{J_x}, \tag{3}$$

19447973, 2024, 4, Downloaded from https://agupubs.onlinelibrary.wiley.com/doi/10.1029/2023WR036023, Wiley Online Library on [03/07/2024]. See the Terms and Conditions (https://onlinelibrary.wiley.com/terms-and-conditions) on Wiley Online Library for rules of use; OA articles are governed by the applicable Creative Commons License

where the sinuosity σ is a function of the Kinoshita curve parameters θ_0, J_f, and J_s, defining the topology of the meander, Π_{H_c} is a dimensionless number that compares the stage at the river relative to the characteristic head drop along a meander, and Π_{J_y} reflects the magnitude and direction (positive for gaining and negative for losing channels) of the RGF, the larger this number, the more important is the modulating role of regional groundwater on the hyporheic exchange process.

2.1.2. Water Age

The age of water (τ; [T]) describes the time of exposure of water and its constituents to the subsurface reactive environment. In particular, the probability distribution function of age, known as the age distribution ($\psi(\mathbf{x}, \tau)$; [T^{-1}]), serves as a proxy metric for the hyporheic zone's biogeochemical potential. From a numerical perspective, it is easier to model the cumulative age distribution ($\Psi(\mathbf{x}, \tau)$; [–]), which is described by the Advection-Dispersion Equation (Ginn, 1999; Gomez & Wilson, 2013), and then estimate the probability distribution function as $\psi(\mathbf{x}, \tau) = \partial\Psi/\partial\tau$. Here, we expand on the mathematical formulation previously proposed by Gomez et al. (2012) and Gomez-Velez et al. (2017) for a vertically-integrated system:

$$\frac{\partial(\epsilon_p (h - Z_b)\Psi)}{\partial\tau} = \nabla\cdot(\mathbf{D}\nabla\Psi) - \nabla\cdot(\mathbf{Q}\Psi) \tag{4}$$

where ϵ_p is porosity [–] and $\mathbf{D} = \{D_{i,j}\}$ is the vertically-integrated dispersion-diffusion tensor [$\mathrm{L}^3\mathrm{T}^{-1}$]. The dispersion-diffusion tensor is defined as

$$D_{i,j} = \alpha_T|\mathbf{Q}|\delta_{i,j} + (\alpha_L - \alpha_T)\,\frac{Q_iQ_j}{|\mathbf{Q}|} + \frac{\epsilon_p H}{\eta}D_m \tag{5}$$

with α_T and α_L the transverse and longitudinal dispersivities [L], respectively, $\delta_{i,j}$ the Kronecker delta function [–], D_m the molecular diffusion [$\mathrm{L}^2\mathrm{T}^{-1}$], and $\eta = \epsilon_p^{-1/3}$ the tortuosity factor approximated with the Millington and Quirk model (Millington & Quirk, 1961).

By definition, water inside the domain has already aged (i.e., $\tau > 0$). Mathematically, this corresponds to $\Psi(x = 0, y, \tau = 0) = 0$. We assume that water entering the alluvial aquifer from the channel (i.e., $\forall\mathbf{x} \in \partial\Omega_c|\quad \mathbf{n}\cdot\mathbf{Q} \le 0$) is "new," and therefore $\Psi(\mathbf{x}, \boldsymbol{\tau}) = 1$. In contrast, we assume water leaving the alluvial aquifer into the channel ($\forall\mathbf{x} \in \partial\Omega_c|\quad \mathbf{n}\cdot\mathbf{Q} > 0$) can be described by an advective boundary condition, that is $-\mathbf{D}\nabla\Psi = 0$. Similar to the flow model, we assume a periodic boundary condition, $\Psi(x = 3L, y, \tau) = \Psi(x = 0, y, \tau)$, for the lateral boundaries ($\mathbf{x} \in \partial\Omega_u \vee \partial\Omega_d$). Finally, we prescribe boundary conditions for the alluvial valley boundary ($\mathbf{x} \in \partial\Omega_v$). Under gaining condition, when water enters the domain from the regional aquifer, we assume that the water age distribution at the boundary is characterized by an exponential distribution $\Psi(\mathbf{x}, \tau) = 1 - \exp(-\tau/\tau_v)$, with a mean age τ_v. Typical values for the mean age of water discharging to rivers from regional groundwater (τ_v) range from one to 10 years (McGuire & McDonnell, 2006). With this in mind, and consistent with Gomez-Velez et al. (2014), we selected $\tau_v = 10$ years for our simulations. On the other hand, under losing conditions, when the water leaves the domain, we assume an advective boundary condition along $\partial\Omega_v$, that is, $-\mathbf{D}\nabla\Psi = 0$.

The net cumulative age distribution for the water leaving the hyporheic zone, also known as the cumulative residence time distribution (CRTD), is estimated by flux-weighting $\Psi(\mathbf{x}, \tau)$ along the boundary where hyporheic water returns to the channel ($\partial\Omega_{c,hz}$):

$$F(\tau) = \frac{\int_{\partial\Omega_{c,hz}}(\mathbf{n}\cdot\mathbf{Q}(\mathbf{x}))\,\Psi(\mathbf{x},\tau)\,\mathrm{d}\mathbf{x}}{\int_{\partial\Omega_{c,hz}}(\mathbf{n}\cdot\mathbf{Q}(\mathbf{x}))\,\mathrm{d}\mathbf{x}}. \tag{6}$$

Finally, Equation 4 can be nondimensionalized by introducing dimensionless age $\tau^* = \tau/\tau_c$, where $\tau_c = \lambda/(KJ_x)$ is a characteristic time scale (see Text S2 in Supporting Information S1 for a detailed derivation).

19447973, 2024, 4, Downloaded from https://agupubs.onlinelibrary.wiley.com/doi/10.1029/2023WR036023, Wiley Online Library on [03/07/2024]. See the Terms and Conditions (https://onlinelibrary.wiley.com/terms-and-conditions) on Wiley Online Library for rules of use; OA articles are governed by the applicable Creative Commons License

Table 1
Microbial Reaction Processes in the Transport Model[a]

Reaction processes	Stoichiometric reaction equation
Aerobic Respiration	$CH_2O + O_2 \rightarrow CO_2 + H_2O$
Nitrification	$O_2 + (^1/_2)NH_4^+ \rightarrow (^1/_2)NO_3^- + H^+ + (^1/_2)H_2O$
Denitrification	$CH_2O + (^4/_5)NO_3^- + (^4/_5)H^+ \rightarrow (^7/_5)H_2O + (^2/_5)N_2 + CO_2$
Microbial NH_4^+ Uptake	$5CH_2O + HCO_3^- + NH_4^+ \rightarrow C_5H_7NO_2 + 4H_2O + CO_2$

[a] Adapted from Gu et al. (2007) and Zarnetske et al. (2012).

2.1.3. Reactive Transport of Solutes Involved in Nitrogen Transformations

The Advection-Dispersion-Reaction Equation (ADRE) describes the spatiotemporal evolution of the reactive solutes involved in nitrogen transformations, including nitrate (NO_3^-; subscript NO), ammonium (NH_4^+; subscript NH), oxygen (O_2; subscript O), and dissolved organic carbon (DOC; subscript C) (Gu et al., 2007; Hunter et al., 1998; Molz et al., 1986; Zarnetske et al., 2012). In particular, we recast the biogeochemical model used by Zarnetske et al. (2012) for the microbially mediated reactions in Table 1 for a vertically-integrated domain:

$$\frac{\partial(\epsilon_p H C_i)}{\partial t} = \nabla\cdot(\mathbf{D}\nabla C_i) - \nabla\cdot(\mathbf{Q}C_i) + \epsilon_p H R_i \tag{7}$$

where $C_i(\mathbf{x}, t)$ and R_i are the concentration [ML^{-3}] and reaction rate [$ML^{-3}T^{-1}$] for species i ($i = NO$, NH, O, or C), respectively. The reaction rates are described by Monod kinetics models (Zarnetske et al., 2012):

$$\begin{aligned} R_O = & -V_O\, y_O\, X_{AR}\left(\frac{C_C}{K_C + C_C}\right)\left(\frac{C_O}{K_O + C_O}\right) \\ & - V_O\left(1 - y_O\right) X_{NIT}\left(\frac{C_{NH}}{K_{NH} + C_{NH}}\right)\left(\frac{C_O}{K_O + C_O}\right), \end{aligned} \tag{8}$$

$$\begin{aligned} R_{NH} = & -V_{NH}\, y_{NH}\, X_{NIT}\left(\frac{C_{NH}}{K_{NH} + C_{NH}}\right)\left(\frac{C_O}{K_O + C_O}\right) \\ & - V_{NH}\left(1 - y_{NH}\right) X_{UP}\left(\frac{C_{NH}}{K_{NH} + C_{NH}}\right)\left(\frac{C_C}{K_C + C_C}\right), \end{aligned} \tag{9}$$

$$\begin{aligned} R_{NO} = & \; V_{NH}\, y_{NH}\, X_{NIT}\left(\frac{C_{NH}}{K_{NH} + C_{NH}}\right)\left(\frac{C_O}{K_O + C_O}\right) \\ & - V_{NO}\, X_{DN}\left(\frac{K_I}{K_I + C_O}\right)\left(\frac{C_C}{K_C + C_C}\right)\left(\frac{C_{NO}}{K_{NO} + C_{NO}}\right), \end{aligned} \tag{10}$$

$$\begin{aligned} R_C = & -V_O\, y_O\, X_{AR}\left(\frac{C_C}{K_C + C_C}\right)\left(\frac{C_O}{K_O + C_O}\right) \\ & - V_{NO}\, X_{DN}\left(\frac{K_I}{K_I + C_O}\right)\left(\frac{C_C}{K_C + C_C}\right)\left(\frac{C_{NO}}{K_{NO} + C_{NO}}\right) \\ & - V_{NH}\left(1 - y_{NH}\right) X_{UP}\left(\frac{C_{NH}}{K_{NH} + C_{NH}}\right)\left(\frac{C_C}{K_C + C_C}\right) \\ & + \frac{\rho_b}{\epsilon_p}\alpha(P - K_d C_C) \end{aligned} \tag{11}$$

where V_i is the maximum microbial process reaction rate [T^{-1}]; X_j is the biomass of the jth functional microbial group [ML^{-3}] facilitating aerobic respiration ($j = AR$), nitrification ($j = NIT$), biological uptake ($j = UP$), or denitrification ($j = DN$); K_I is the inhibition constant for the denitrification reaction [ML^{-3}]; K_i is the half-saturation constant [ML^{-3}], ρ_b is the sediment bulk density [ML^{-3}], and y_O and y_{NH} are the dimensionless partition coefficients for oxygen and ammonium, respectively. These partition coefficients depend on the reaction

19447973, 2024, 4, Downloaded from https://agupubs.onlinelibrary.wiley.com/doi/10.1029/2023WR036023, Wiley Online Library on [03/07/2024]. See the Terms and Conditions (https://onlinelibrary.wiley.com/terms-and-conditions) on Wiley Online Library for rules of use; OA articles are governed by the applicable Creative Commons License

of interest. More specifically, the partition coefficient for the oxygen demand process (y_O) is based on the known free energy yield between the two competing processes of aerobic respiration and nitrification Zarnetske et al. (2012). On the other hand, the ammonium partition coefficient (y_{NH}) is based on the bioenergetics and bacteria growth efficiencies (Zarnetske et al., 2012).

Finally, this model assumes that the dissolution of particulate organic carbon (POC, P) [M $\mathrm{M}_{\mathrm{sediment}}^{-1}$] is described by an irreversible, first-order process (Jardine et al., 1992; Robertson & Cherry, 1995):

$$\frac{\partial P}{\partial t} = -\alpha(P - K_d C_C), \tag{12}$$

where α is the first-order mass transfer coefficient [T^{-1}], K_d is the linear distribution coefficient for the sediment ($\mathrm{L}^3\mathrm{M}_{\mathrm{sediment}}^{-1}$).

Initial and boundary conditions are needed to complete the mathematical statement. An initial distribution of dissolved solutes ($C_i(\mathbf{x}, t = 0) = C_{i,0}(\mathbf{x})$) and POC ($P(t = 0) = P_0$) are prescribed. Because our focus is on the long-term behavior of the alluvial aquifer under the assumption of time-invariant flow, we explore the spatial distribution of reactive species after it reaches a steady-state equilibrium, where initial conditions are irrelevant. With this in mind, we can assume $C_i(\mathbf{x}, t = 0) = 0$. In the following, we will further specify this model.

Boundary conditions along the meandering channel depend on flow direction. The concentration of dissolved species in rivers can have important and large variations in space and time (e.g., DOC and DO (Creed et al., 2015; Diamond et al., 2023), respectively). To reduce the complexity of our model, for water entering the alluvial aquifer from the channel (i.e., $\{\forall \mathbf{x} \in \partial\Omega_c | \quad \mathbf{n} \cdot \mathbf{Q} < 0\}$), we prescribe constant concentrations for all the dissolved species ($C_i = C_{i,c}$). On the other hand, for water leaving the alluvial aquifer and discharging into the channel (i.e., $\{\forall \mathbf{x} \in \partial\Omega_c | \quad \mathbf{n} \cdot \mathbf{Q} > 0\}$), we assume an advective boundary condition of the form $-\mathbf{n} \cdot (-\mathbf{D}\nabla C_i) = 0$. A periodic boundary condition is assumed for the lateral boundaries ($\mathbf{x} \in \partial\Omega_u \vee \partial\Omega_d$), where the spatial distribution of the solute concentration along the upstream and downstream boundaries satisfies $C_i(x = 3L, y) = C_i(x = 0, y)$. Finally, the conditions along the alluvial valley boundary ($\mathbf{x} \in \partial\Omega_v$) depend on the RGF direction. Under neutral conditions ($J_y = 0$), we impose a no-flux boundary condition, $-\mathbf{n} \cdot (\mathbf{Q}C_i - \mathbf{D}\nabla C_i) = 0$. Under gaining conditions ($J_y > 0$), we prescribe constant concentrations for all the dissolved species ($C_i = C_{i,v}$). And, under losing conditions ($J_y < 0$), we assume an advective boundary condition of the form $-\mathbf{n} \cdot (-\mathbf{D}\nabla C_i) = 0$.

To gain some perspective on the characteristic time scale for POC dissolution, we explore the following scenario. The maximum dissolution rate for POC is reached when $C_C = 0$, resulting in a simplified version of Equation 12:

$$\frac{\mathrm{d}P}{\mathrm{d}t} = -\alpha P \tag{13}$$

The solution to this ordinary differential equation is given by $P(t) = P_0 \exp(-\alpha t)$, with P_0 the initial concentration of POC within the sediment. In this case, $t_{c,POC} = \alpha^{-1}$ is a characteristic time scale for the dissolution of POC, which typically varies within the range 0.1–10 years (Zarnetske et al., 2012). In other words, the time required for a 10% decrease of the original POC available can be calculated as $t_{10\%} = -t_{c,POC} \ln(0.1)$, resulting in approximately 0.23–23 years. Again, this is a low-end estimate of the dissolution time scale, which is expected to be significantly longer given the availability of DOC. Furthermore, this estimate is consistent with the relatively recalcitrant nature of POC, and it is likely longer given the potential for replenishment of POC by hydrologic events taking place at time scales shorter of the order of magnitude of $t_{10\%}$ (see, e.g., Gu et al., 2007). Based on these arguments, it is reasonable to assume that the change in POC concentration within the alluvium is insignificant during the modeling time scales (i.e., $P(t) \approx P_0$). This approximation simplifies the reaction rate for DOC, where the contribution of POC (see last term in Equation 11) can be replaced by $(\alpha\rho_b/\epsilon_p)$ $(P_0 - K_d C_C)$. We validated this assumption with a series of one-dimensional numerical experiments using typical values of the coefficients involved in the model. In this case, we solved the system of PDEs from Equations 7–11, which is transient in nature and accounts for the coupled dissolution of POC, and compare its long-term solution with the steady-state version of these equations, where $\partial(\epsilon_p H C_i)/\partial t \to 0$ and $P(t) = P_0$. Both solutions converge to the same concentrations (see Figure S1 in Supporting Information S1 for an example.)

19447973, 2024, 4, Downloaded from https://agupubs.onlinelibrary.wiley.com/doi/10.1029/2023WR036023, Wiley Online Library on [03/07/2024]. See the Terms and Conditions (https://onlinelibrary.wiley.com/terms-and-conditions) on Wiley Online Library for rules of use; OA articles are governed by the applicable Creative Commons License

19447973, 2024, 4, Downloaded from https://agupubs.onlinelibrary.wiley.com/doi/10.1029/2023WR036023, Wiley Online Library on [03/07/2024]. See the Terms and Conditions (https://onlinelibrary.wiley.com/terms-and-conditions) on Wiley Online Library for rules of use; OA articles are governed by the applicable Creative Commons License

Similar to the flow and water age models, we nondimensionalize the biogeochemical model. In addition to the dimensionless variables defined in Equation 3, the solution to this fully-coupled system of PDEs only depends on the values of 18 dimensionless variables (see Text S2 in Supporting Information S1 for a detailed derivation). First, a series of Damköhler numbers (Da_i) comparing the role of reaction and transport processes (expressed as the ratio of time scales characterizing advective transport and biogeochemical transformations) of the ith constituent (Oldham et al., 2013):

$$Da_O = \frac{V_O \lambda}{K J_x}, Da_{NO} = \frac{V_{NO} \lambda}{K J_x}, Da_{NH} = \frac{V_{NH} \lambda}{K J_x}, Da_P = \frac{\alpha \lambda}{K J_x} \tag{14}$$

Transformation in systems where $Da_i \gg 1$ are likely limited by the transport of critical constituents (i.e., the supply) relative to the reaction demand. We refer to these systems as reaction-dominated or transport limited. In contrast, transformations in systems with $Da_i \ll 1$ are limited by the reaction rate. We refer to these systems as transport-dominated or reaction-limited.

Second, a series of dimensionless channel concentrations:

$$\Pi_{C,c} = \frac{C_{C,c}}{C_{O,c}}, \Pi_{NH,c} = \frac{C_{NH,c}}{C_{O,c}}, \Pi_{NO,c} = \frac{C_{NO,c}}{C_{O,c}}, \Pi_{P-C} = \frac{\rho_b P_0}{\epsilon_p C_{C,c}} \tag{15}$$

and alluvial valley concentrations:

$$\Pi_{O,v} = \frac{C_{O,v}}{C_{O,c}}, \Pi_{C,v} = \frac{C_{C,v}}{C_{O,c}}, \Pi_{NH,v} = \frac{C_{NH,v}}{C_{O,c}}, \Pi_{NO,v} = \frac{C_{NO,v}}{C_{O,c}} \tag{16}$$

The dimensionless concentrations for the channel and the alluvial valley boundary ($\Pi_{i,c}$ and $\Pi_{i,v}$) ith chemical constituent are scaled by channel oxygen concentration $C_{O,c}$. In particular, the dimensionless parameter $\Pi_{C,c} = C_{C,c}/C_{O,c}$ plays a central role in the denitrification process because it dictates the availability of oxygen and DOC for the aerobic respiration reaction within the hyporheic zone. This, at the same time, becomes a critical control in the nitrification and denitrification reactions that depend on this respiration reaction (see Table 1). In other words, $\Pi_{C,c}$ is a master variable critical to identify the biogeochemical potential of hyporheic zones to process nitrate. If $\Pi_{C,c} > 1$, the reaction will be limited by the availability of oxygen, and we refer to these systems as oxygen-limited. On the other hand, if $\Pi_{C,c} < 1$, the availability of carbon limits the aerobic respiration process, and we refer to the system as carbon-limited. Among these dimensionless concentrations, the dimensionless initial POC content in the alluvium ($\Pi_{P-C} = (\rho_b P_0)/(\epsilon_p C_{C,c})$) is particularly important. Π_{P-C} can be understood as the ratio of the mass of carbon stored as POC per unit volume of alluvium to the maximum mass of carbon as DOC in the pores per unit volume of alluvium. The larger this number, the higher the potential of POC dissolution to offset the carbon limitation observed in systems with $\Pi_{C,c} < 1$. With this in mind, Π_{P-C} becomes a master dimensionless variable to evaluate the biogeochemical potential of hyporheic exchange.

Third, a series of dimensionless half-saturation (Π_{K_i}), inhibition (Π_{K_I}), and POC linear distribution (Π_{K_d}) coefficients:

$$\Pi_{K_C} = \frac{K_C}{C_{O,c}}, \Pi_{K_O} = \frac{K_O}{C_{O,c}}, \Pi_{K_{NH}} = \frac{K_{NH}}{C_{O,c}}, \Pi_{K_{NO}} = \frac{K_{NO}}{C_{O,c}}, \Pi_{K_I} = \frac{K_I}{C_{O,c}}, \Pi_{K_d} = \frac{K_d C_{O,c}}{P_0} \tag{17}$$

2.2. Selection of Scenarios: Exploring the Parameter Space

In the following, we describe the approach used to generate the simulation scenarios. In this case, we vary the meander topology and model parameters. In total, we performed 10,200 numerical simulations.

2.2.1. Meander Topology

The maximum angular amplitude (θ_0), flatness (J_f), and skewness (J_s) parameters of the Kinoshita curve (Equation 1) offer enough flexibility to capture the key aspects of the forms observed in single meanders (Seminara, 2006). Here, we explored the parameter space ($\theta_0 \in [30, 120]$, $J_s \in [0, 10]$, and $J_f \in [0, 10]$) to

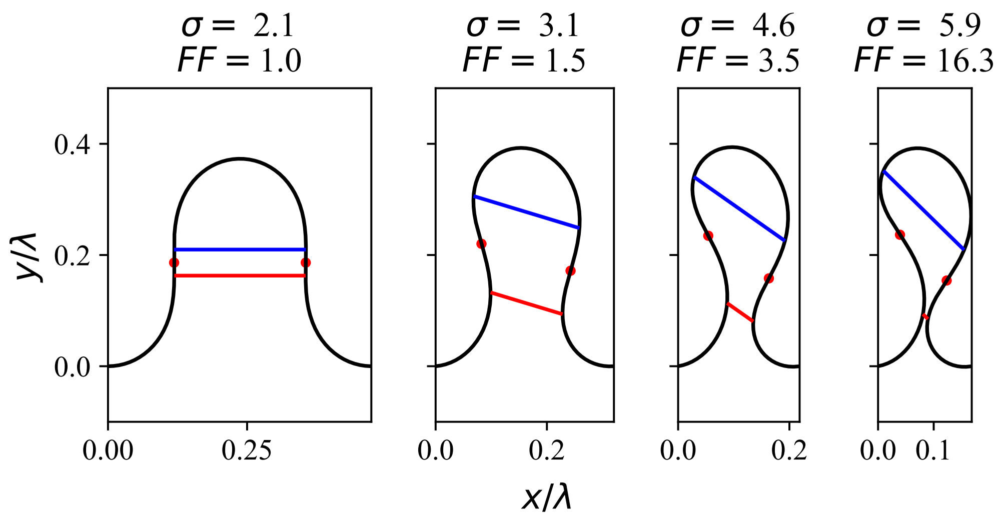

Figure 2. *Meander topologies used in the analysis*. Four Kinoshita topologies generated with parameters, from left to right, θ_0 = [90, 105, 115, 120]°, J_s = [0, 0.014, 0.020, 0.020], and J_f = [0.0048, 0, 0, 0]. Axes are in dimensionless coordinates $x^* = x/\lambda$ and $y^* = x/\lambda$, resulting in meanders with a unitary dimensionless arc wavelength. The red dots denote the inflection points, and the dashed lines represent the characteristic lengths of the meander neck (red) and lobe (blue). These lengths are estimated as the longest distance within the neck or lobe along a line parallel to the line defined by the inflection points. Each meander shows the sinuosity (σ) and funneling factor (FF).

reproduce four types of meander planimetry similar to the ones studied by Revelli et al. (2008). As shown for the selected topologies in Figure 2, we progressively increased the sinuosity from 2.1 to 5.9, and the size of the meander neck (dashed red line) decreases with increasing θ_0, while the degree of symmetry decreases with increasing skewness. To assess the importance of the meander neck, which significantly impacts the hydrodynamics of hyporheic exchange and biogeochemical transformation, we define the funneling factor (FF) $FF = L_n/L_l$, where L_n and L_l are the maximum distances within the meander neck and lobe, respectively, of lines parallel to the line defined by the meander inflection points. High FF values correspond to meanders with narrow necks and significant lobe space.

It is important to note that the topologies in Figure 2 are shown in the dimensionless space $x^* = x/\lambda$ and $y^* = x/\lambda$, and therefore have a unitary channel length (i.e., arc wavelength). However, because the Kinoshita curve scales linearly with arc wavelength, we can obtain a meander with any value of λ without changing the topology simply by multiplying the axes x^* and y^* by a factor of λ.

2.2.2. System Parameters

Central to our analysis is the selection of scenarios that span a parameter space representative of natural systems. Values for all the parameters involved in our models can be found in the literature (e.g., Bekins et al., 1998; Deng et al., 2015; Dwivedi et al., 2018; Green et al., 2018; Gu et al., 2007, 2008a, 2008b, 2012; Hedin et al., 1998; Hester et al., 2014; Liao et al., 2012; Lindsey et al., 2003; Sawyer, 2015; Stelzer & Bartsch, 2012; Zarnetske et al., 2012; L. Zheng et al., 2016). However, reported values typically consist of a handful of observations or only a range, limiting our ability to establish correlations or empirical probability distributions. To partially address this issue, we use a Monte Carlo (MC) simulation approach to assess the variability of the dimensionless parameters controlling the flow, transport, and reaction models.

Our MC analysis generates 10,000 independent random realizations of each parameter to calculate 10,000 random realizations of the dimensionless parameters. These realizations are then used to propose a probability density function (PDF) for each dimensionless parameter. For some parameters, we have enough data to obtain an empirical PDF (see below). However, in several cases, especially for critical biogeochemical parameters, we only have information about the typical ranges reported in the literature. Therefore, we assume an “uninformative” uniform distribution bounded by the reported range in these cases. If the parameter varies over orders of magnitude, we assumed that the logarithm of the parameter was uniformly distributed.

19447973, 2024, 4, Downloaded from https://agupubs.onlinelibrary.wiley.com/doi/10.1029/2023WR036023, Wiley Online Library on [03/07/2024]. See the Terms and Conditions (https://onlinelibrary.wiley.com/terms-and-conditions) on Wiley Online Library for rules of use; OA articles are governed by the applicable Creative Commons License

Table 2
Parameters for the Monte Carlo Analysis

Symbol	Range	Domain	Distribution	Units
J_x[a]	10^{-5}–73.36	Logarithmic	ECDF	–
K[b]	10^{-10}–$10^{-3.3}$	Logarithmic	ECDF	m s^{-1}
λ[c]	1–4.70	Logarithmic	Uniform	m s^{-1}
$C_{O,c}$[d,e]	0–20	Linear	ECDF	mg L^{-1}
$C_{NH,c}$[f]	0.05–5	Logarithmic	Uniform	mg L^{-1}
$C_{NO,c}$[d]	0–19.6	Linear	ECDF	mg L^{-1}
$C_{C,c}$[d]	0.1–171	Logarithmic	ECDF	mg L^{-1}
P_0[g]	10^{-6}–0.02	Logarithmic	Uniform	mg mg^{-1}
V_O[f]	0.1–10	Logarithmic	Uniform	h^{-1}
V_{NH}[f]	0.36–4.2	Logarithmic	Uniform	h^{-1}
V_{NO}[f]	0.26 to 10	Logarithmic	Uniform	h^{-1}
α[f]	10^{-5}–10^{-3}	Logarithmic	Uniform	h^{-1}
K_O[f]	0.2–5.8	Logarithmic	Uniform	mg L^{-1}
K_{NH}[f]	0.1–1.1	Logarithmic	Uniform	mg L^{-1}
K_{NO}[f]	0.21–3.1	Logarithmic	Uniform	mg L^{-1}
K_C[f]	1–10	Logarithmic	Uniform	mg L^{-1}
K_d[f]	5–100	Logarithmic	Uniform	L mg^{-1}
K_I[f]	0.2–1	Logarithmic	Uniform	mg L^{-1}

Note. This table includes information on the typical range of the parameter and the probability distribution function used for the generation of independent realizations. *ECDF* is the Empirical Cumulative Distribution Function, and *Uniform* is a uniform probability distribution function (i.e., uninformative prior). [a]Moore et al. (2019). [b]Hill et al. (2016). [c]NHDPlus High-Res data set. [d]Sterle et al. (2024). [e]Oxygen concentration higher than 20 mg/L are removed. [f]Zarnetske et al. (2012). [g]From Gu et al. (2007), Sawyer (2015), and Zarnetske et al. (2012).

For channel slope (J_x), channel DOC ($C_{C,c}$), oxygen concentrations ($C_{C,c}$), nitrate concentration ($C_{NO,c}$), and hydraulic conductivity (K), we propose empirical PDFs with values reported for the conterminous US (CONUS). First, values for J_x and mean annual discharge (Q_{ma}) were taken from the NHD Plus High-Resolution data set (Moore et al., 2019). Oxygen, DOC, and nitrate concentrations were obtained from the CAMELS-Chem data set, provided in Sterle et al. (2024). Values of oxygen concentration higher than 20 mg/L were removed because it is uncommon to find natural channels with such a high concentration; they account for less than 0.001% of the data set. Hydraulic conductivity values were taken from the StreamCat database version 2 (Hill et al., 2016), which reports mean reach catchment lithological hydraulic conductivity. Finally, all the other parameters were explored with a uniform distribution. Table 2 summarizes these ranges. The probability distribution functions for the input parameters are shown in Figures S4–S7 in Supporting Information S1; and the resulting probability distribution functions are shown in Figures S8 and S9 in Supporting Information S1.

To explore the effects of RGF, we simulated scenarios with $\Pi_{J_y} = J_y / J_x \in [-10, -1, 0, 1, 10]$, covering neutral, gaining, and losing conditions. Consistent with our MC analysis, we also analyzed a wide range of oxygen Damkhöler numbers, covering reaction-limited systems ($Da_O \in [10^{-2}, 1]$) and transport-limited or supply-limited systems ($Da_O \in (1, 10^{14}]$). Similarly, we explored Π_C values representative of covered carbon-limited ($\Pi_C \in [10^{-2}, 1)$) and oxygen-limited ($\Pi_C \in (1, 10^2]$) systems. In general, Da_O and Π_C can be understood as master variables that dictate the consumption of oxygen through aerobic respiration, which, at the same time, constraining the reaction ladder leading to the progression of nitrification, denitrification, and uptake (Table 1).

Lastly, we evaluated two scenarios of the channel concentrations for nitrate (NO_3^-) and ammonium (NH_4^+). Like L. Zheng et al. (2016), we explored a pristine channel with $C_{NO} = 1$ mg/L and $C_{NH} = 0.05$ mg/L and a contaminated channel with $C_{NO} = 8$ mg/L and $C_{NH} = 5$ mg/L. We also explored three cases for POC concentration: $P_0 = [0, 0.02, 0.2]$%. POC within the alluvial aquifer can offset the DOC limitations, enhancing biogeochemical transformations (Sawyer, 2015).

To reduce the parameter space, we assume the ratios V_{NO}/V_O and V_{NH}/V_O are relatively stable for most alluvial systems. In other words, for the purposes of our analyses, we assume that these ratios, and therefore, the ratios of their corresponding Da numbers (Equation 14) are constant. Figures S10 and S11 in Supporting Information S1 show the distribution of these ratios from our MC realizations. In this case, we compared the MC-derived PDF and its mean value with the values reported by Zarnetske et al. (2012) ($V_O = 1.97$ hr^{-1}, $V_{NH} = 1.08$ hr^{-1}, and $V_{NO} = 3.98$ hr^{-1}). The simulated mean ratios are close to the ratios from Zarnetske et al. (2012).

Now, for the half-saturation constants, we assumed that the ratio of the Monod Kinetics term remains relatively constant. This ratio can be expressed in terms of the metric $M_i = [(K_O/C_{O,c}) + 1][(K_i/C_{i,c}) + 1]$ with $i = C, NH, NO$. The MC-derived PDFs are consistent with the estimates with the values reported by Zarnetske et al. (2012) ($K_{DOC} = 8.68$ mg/L, $K_{NH} = 0.43$ mg/L, and $K_{NO} = 1.64$ mg/L).

3. Results and Discussion

In the following, we use our modeling framework to explore the role of meander topology (the exchange driver), RGF (the exchange modulator), and alluvium physical and biogeochemical properties of sinuosity-driven hyporheic exchange and its potential for biogeochemical transformations. To this end, we use the key dimensionless variables described in Section 2 (and derived in Supporting Information S1), which provide master variables to characterize the exchange process in terms of widely available hydrogeomorphic parameters and

19447973, 2024, 4, Downloaded from https://agupubs.onlinelibrary.wiley.com/doi/10.1029/2023WR036023, Wiley Online Library on [03/07/2024]. See the Terms and Conditions (https://onlinelibrary.wiley.com/terms-and-conditions) on Wiley Online Library for rules of use; OA articles are governed by the applicable Creative Commons License

19447973, 2024, 4, Downloaded from https://agupubs.onlinelibrary.wiley.com/doi/10.1029/2023WR036023, Wiley Online Library on [03/07/2024]. See the Terms and Conditions (https://onlinelibrary.wiley.com/terms-and-conditions) on Wiley Online Library for rules of use; OA articles are governed by the applicable Creative Commons License

water quality observations. Using these master variables is critical to gaining mechanistic understanding, transferability, and the integration of this mechanism into future generations of water quality models.

3.1. Meander Topology Drives Hyporheic Exchange and Conditions the Modulating Effects of Regional Groundwater Flow

First, we focus on the exchange hydrodynamics, specifically, the interplay between two master dimensionless variables: σ and Π_{J_y}. The former corresponds to sinuosity, which encapsulates the Kinoshita curve parameters, and the latter represents the magnitude and direction (positive for gaining and negative for losing channels) of the RGF.

3.1.1. Implications for Flow

We performed systematic simulations of the exchange process spanning typical ranges for the dimensionless master variables for flow. The results, summarized in Figures 3 and 4, include four sinuosity values ($\sigma = 2.1$, 3.1, 4.6, and 5.9), which correspond to significant changes in the FF (respectively, $FF = 1.0$, 1.5, 3.5, and 16.3), and five Π_{J_y} values. The Π_{J_y} values represent RGF parallel to the channel axis ($\Pi_{J_y} = 0$), which we refer to as neutral conditions, moderate gaining ($\Pi_{J_y} = 1$) and losing ($\Pi_{J_y} = -1$) RGF, and strongly gaining ($\Pi_{J_y} = 1$) and losing ($\Pi_{J_y} = -1$) RGF. All simulations have unitary dimensionless channel wavelength (i.e., dimensionless distance along the channel).

Changes in the master variables result in significant changes in the velocity field (colors in Figure 3) and extent of the sinuosity-driven hyporheic zone (area delimited by the black streamlines in Figure 3). Under neutral conditions ($\Pi_{J_y} = 0$, third row in Figure 3), all the sinuosity scenarios (columns) have important commonalities: (a) the hyporheic zone extends slightly into the alluvial valley, (b) the highest fluxes occur along neck flow paths, and (c) the lowest fluxes occur within the lobe. However, as sinuosity increases and the neck narrows (increasing FF), the magnitude of the flux along neck flow paths significantly increases due to the higher hydraulic gradients. Previous work by Boano, Demaria, et al. (2010) and Revelli et al. (2008) show similar zonation and highlight its importance for constraining the dominant transport time scales within the meander and, therefore, the potential for specific biogeochemical transformation. For example, flow paths along the lobe are more likely to contribute to processes that require long time scales such as methanogenesis (e.g., Baker et al., 1999; Dahm et al., 1998). In contrast, neck flow paths have shorter time scales for reactions to take place but are likely enough to control aerobic respiration and denitrification processes (e.g., Boano, Demaria, et al., 2010). Note that except for the studies mentioned above, most previous work has focused on low sinuosity meanders where the neck does not impact the timescales (e.g., Cardenas, 2009a, 2009b; Gomez et al., 2012; Gomez-Velez et al., 2017).

We explore four conditions where RGF has a component perpendicular to the channel axis: moderate gaining ($\Pi_{J_y} = 1$) and losing ($\Pi_{J_y} = -1$) and strong gaining ($\Pi_{J_y} = 10$) and losing ($\Pi_{J_y} = -10$). In this case, the hyporheic zone is compressed, and in some cases, it does not develop (rows 1, 2, 4, and 5 in Figure 3). Low sinuosity channels ($\sigma = 2.1$; first column in Figure 3) are susceptible to the compressing effect of RGF. For example, for moderate RGF conditions ($\Pi_{J_y} = \pm 1$), the extent of the hyporheic zone decreases by about 30%, and a more significant proportion of the hyporheic zone is within the meander lobe. When this flux is further increased ($\Pi_{J_y} = \pm 10$), the exchange zone almost disappears, becoming confined to a small fraction of the meander lobe. These flow field changes reflect significant reductions in the total amount of water circulating through the hyporheic zone. For example, for $\sigma = 2.1$, the total hyporheic exchange flux can be reduced by a factor of 1.7 for moderate conditions and as much as a factor of 70 for strong conditions (Equation 4). As sinuosity (and FF) increases, the compressing effect of regional gaining and losing conditions decreases (cases with $|\Pi_{J_y}| > 0$ and $3.1 \leq \sigma \leq 5.9$ in Figure 3). The meander neck offers a hydrodynamic shielding effect that protects the hyporheic zone, maintaining its general flow patterns and decreasing the differences in the total amount of hyporheic exchange (Figure 4).

Our findings highlight the critical role of meander topology to drive exchange and counteract the modulating effect of RGF. This aspect has not been revealed in previous studies (e.g., Boano, Demaria, et al., 2010; Revelli et al., 2008), where RGF was not represented. Channels with low FF and sinuosity are characterized by a fragile hyporheic zone that easily disappears under the influence of RGF. This behavior is consistent with previous

19447973, 2024, 4, Downloaded from https://agupubs.onlinelibrary.wiley.com/doi/10.1029/2023WR036023, Wiley Online Library on [03/07/2024]. See the Terms and Conditions (https://onlinelibrary.wiley.com/terms-and-conditions) on Wiley Online Library for rules of use; OA articles are governed by the applicable Creative Commons License

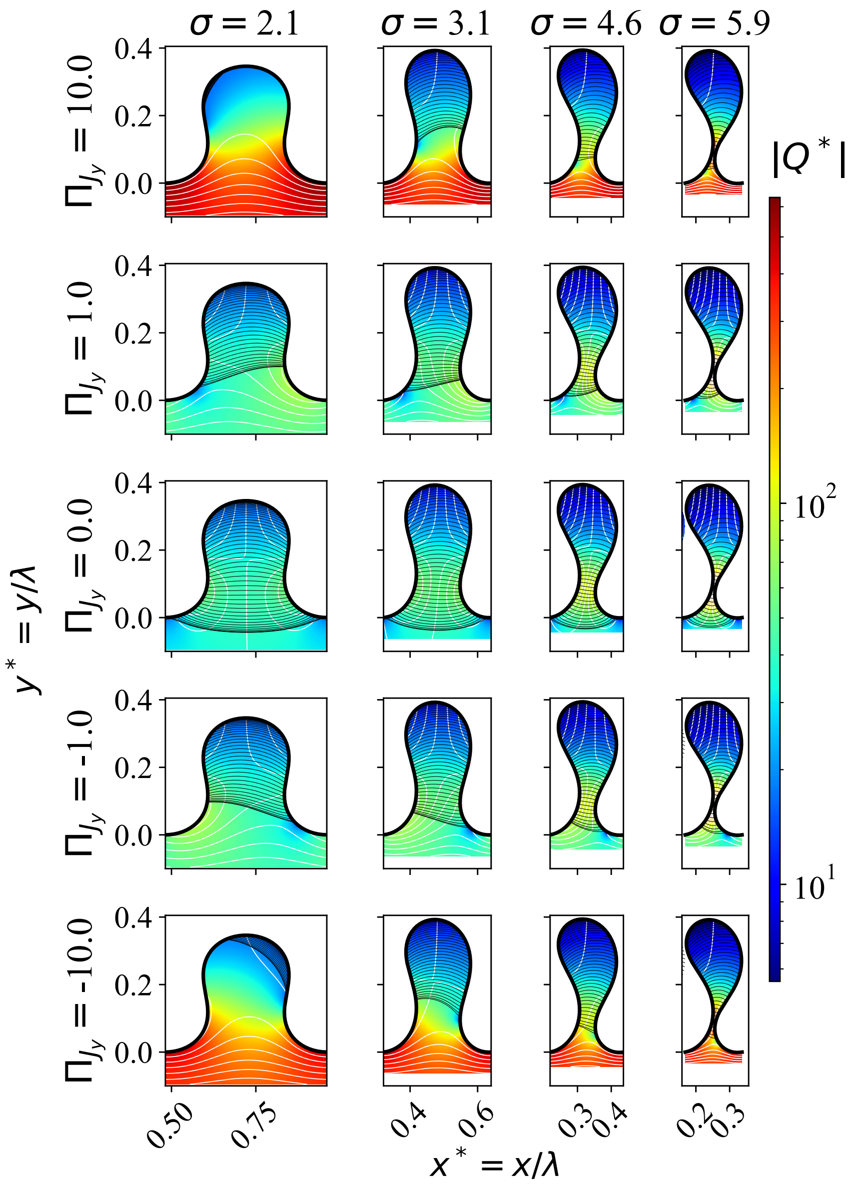

Figure 3. *Flow field and sinuosity-driven hyporheic zone within the alluvial aquifer*. The magnitude of the dimensionless flux (**Q***; colors), dimensionless hydraulic head (white contours), and hyporheic streamlines (black lines) for four meander topologies (columns) under neutral ($\Pi_{J_y} = 0$), moderate ($\Pi_{J_y} = 1$), and strong ($\Pi_{J_y} = 10$) regional groundwater flow conditions (rows).

contributions by Cardenas (2009b) and Gomez-Velez et al. (2017). In contrast, channels with more significant funneling factors (and sinuosity) form a hydrodynamic shield that protects the sinuosity-driven hyporheic zone. Previous efforts to assess the cumulative biogeochemical potential of meanders along river corridors (e.g., Gomez-Velez & Harvey, 2014; Gomez-Velez et al., 2015, 2017; Kiel & Bayani Cardenas, 2014) likely underestimate the importance of sinuosity-driven hyporheic exchange, which is more robust than previously thought.

3.1.2. Implications for Transport Time Scales

Changes in the flow field result in changes in water residence time, which is a proxy for the time that solutes interact with the reacting environment and, therefore, for the biogeochemical potential within the hyporheic zone (Gomez & Wilson, 2013). We modeled the flux-weighted CRTD for the sinuosity-driven hyporheic zone. This distribution measures the characteristic time scales for hyporheic water discharging to the channel. While this is

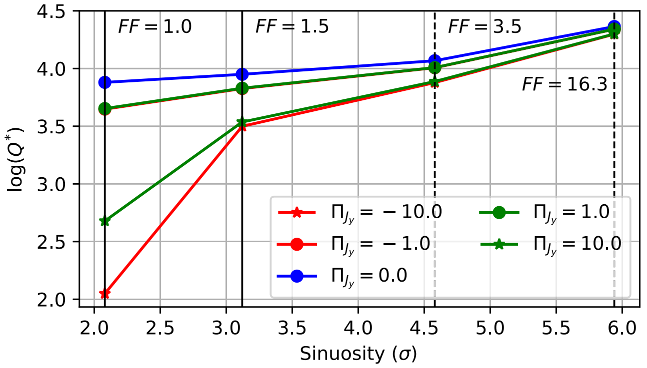

Figure 4. *Total dimensionless hyporheic exchange flux (Q^*) as a function of meander topology (σ) and regional groundwater flow (Π_{J_y}).* The funneling factor (*FF*) for each meander topology is included as a reference. Also, notice that the green solid line ($\Pi_{J_y} = 1$) is on top of the red line ($\Pi_{J_y} = -1$).

not the only constraint on reactivity, it is a fundamental metric that deserves attention. In particular, because it provides insight into the changes in transport mechanisms, in the following subsection, we summarize the results of a more detailed exploration of the biogeochemical transformation and the balance between residence times and reaction time scales.

As expected, increasing the FF (or sinuosity) shifts the CRTD left toward younger residence times (compare blue and red curves in Figure 5). This shift is expected because the relative contribution of meander neck flow paths, which have younger water, to the total exchange increases as sinuosity increases. For example, the median residence time for a meander with $\sigma = 5.9$ (blue lines in Figure 5) are about two orders of magnitude younger than the ones observed in low-sinuosity meanders ($\sigma = 2.1$, red lines in 5).

Interestingly, increasing the RGF has relatively minor effects on the overall shape of the CRTD (notice the variability between lines of the same color, which correspond to different values of Π_{J_y}, in Figure 5). Differences are minimal for high-sinuosity cases, where the hyporheic zone is only slightly affected by the RGF. For example, for $\sigma = 5.9$, increasing RGF shifts the CRTD toward younger ages. In this case, the outer hyporheic flow paths within the alluvium are compressed (see the last column of Figure 3). Because these flow paths have lower velocities and travel longer distances, their removal results in a slightly younger CRTD. In other words, the role of the meander neck and its overall contribution to the total exchange flux is enhanced.

Meanders with $\sigma = 3.1$ and 4.6 behave somewhat differently because some of their neck flow paths are removed by the RGF, leading to an enhanced role of older residence times within the meander lobe. For example, when these meanders are exposed to moderate RGF (dashed lines in Figure 5), their CRTD is biased toward younger residence times. This bias is explained by the prevalence of neck flow paths, which remain dominant (see second and fourth rows in Figure 3). However, under strong RGF ($|\Pi_{J_y}| = 10$), a more significant fraction of the neck flow paths are removed, resulting in a higher relative contribution of older water from the meander lobe and a shift the CRTD toward older residence times (see dashed lines with stars in Figure 5).

For the lowest sinuosity ($\sigma = 2.1$), the neck flow paths are readily removed under the modulating effect of RGF. In the case of strong RGF, only a small hyporheic zone with short flow paths and low velocities remains (see first and

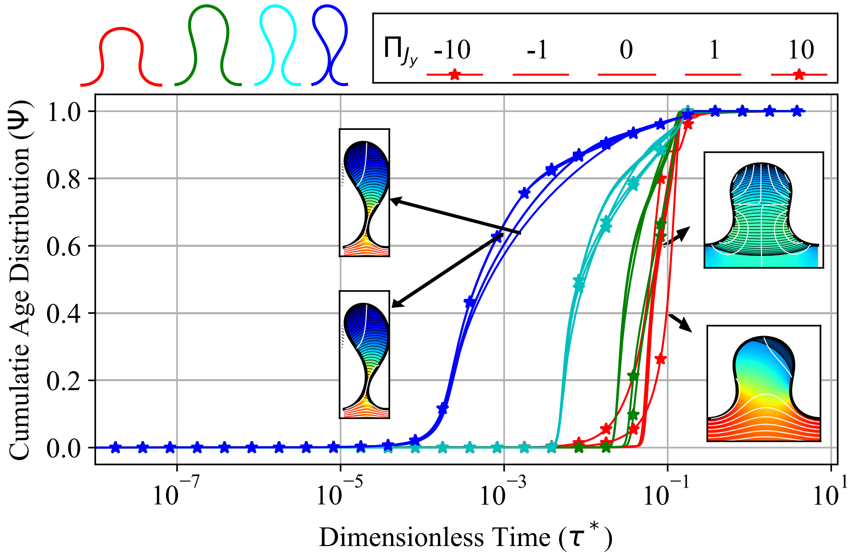

Figure 5. *Cumulative residence times (CRTD).* CRTD of all meander topologies separated by the colors shown above, the line styles denote the stream conditions, from strong gaining ($\Pi_{J_y} = 10$) to strong losing ($\Pi_{J_y} = -10$) conditions, passing through neutral conditions ($\Pi_{J_y} = 0$).

19447973, 2024, 4, Downloaded from https://agupubs.onlinelibrary.wiley.com/doi/10.1029/2023WR036023, Wiley Online Library on [03/07/2024]. See the Terms and Conditions (https://onlinelibrary.wiley.com/terms-and-conditions) on Wiley Online Library for rules of use; OA articles are governed by the applicable Creative Commons License

19447973, 2024, 4, Downloaded from https://agupubs.onlinelibrary.wiley.com/doi/10.1029/2023WR036023, Wiley Online Library on [03/07/2024]. See the Terms and Conditions (https://onlinelibrary.wiley.com/terms-and-conditions) on Wiley Online Library for rules of use; OA articles are governed by the applicable Creative Commons License

last row in the first column of Figure 3). This compression of the hyporheic zone results in younger residence times for low quantiles and older residence times for higher quantiles (Figure 5).

Previous efforts have highlighted the dominant role of neck flow paths in residence times distributions (Boano, Demaria, et al., 2010; Revelli et al., 2008). However, these studies did not assess the role of RGF. On the other hand, Cardenas (2009b) and Gomez-Velez et al. (2017) represent the role of RGF but only explore low-sinuosity meanders. Here, we demonstrate the critical interplay between these two factors and how they affect transport time scales. Furthermore, it is important to highlight that while the effects of RGF in the CRTD are minor for moderate sinuosity, the changes in the total amount of exchange flux can be one to two orders of magnitude. In other words, two systems with the same sinuosity and different values of Π_{J_y} will have similar characteristic time scales for transport, but very different amounts of water (and solutes) will be exposed to the hyporheic reactive environment.

3.2. The Biogeochemical Potential of Sinuosity-Driven Hyporheic Zones

Flow and residence time are critical indicators of the potential for biogeochemical transformation; however, realizing this potential strongly depends on the reactions considered and their biogeochemical time scales. To further explore this issue, we focused our analysis on nitrogen transformations (see Table 1), and in particular on the net biogeochemical function of sinuosity-driven hyporheic zones to remove or produce nitrate (NO_3^-; subscript NO in our model), given the widespread excess in streams and rivers across the globe (Dodds et al., 2013; Smith et al., 2003).

Our simulations are spatially explicit; however, to evaluate the net biogeochemical potential of sinuosity-driven hyporheic zones, we conceptualize this exchange zone as a biogeochemical reactor that processes inputs from the channel and delivers outputs back to the channel. With this aggregate perspective, we define the net biogeochemical potential for a constituent i (e.g., NO_3^-, NH_4^+, O_2, and DOC) as the net mass of the constituent removed ($P_i > 0$) or produced ($P_i < 0$) within the reactor relative to the input mass. Mathematically, this is given by

$$P_i = \frac{M_{i,in} - M_{i,out}}{M_{i,in}} = 1 - \frac{M_{i,out}}{M_{i,in}} \tag{18}$$

where $M_{i,in}$ and $M_{i,out}$ are the mass of constituent i entering and leaving the hyporheic zone, respectively.

We illustrate the spatial variation of the biogeochemical potential for nitrate (P_{NO}) by estimating the metric along flow paths (Figure 6). In this case, we explore eight scenarios with varying sinuosity and Da_O, which highlights the complex interplay between transport and biogeochemical time scales, substrate availability, and sinuosity. For example, systems with high Da_O values ($Da_O = 10^8$) are characterized by hyporheic flow paths with plenty of contact time with the reactive environment and, therefore, a tendency to fully consume the nitrate recharged from the channel within a short distance. When we aggregate the contribution from all the flow paths leaving the hyporheic zone, these meanders behave as a net sink for nitrate. In contrast, hyporheic flow paths in meanders with low Da_O ($Da_O = 10^4$) take longer distances to transition from source (red) to sink (blue). In fact, increasing sinuosity results in flow paths crossing the meander neck that remain as a sink (meander with $\sigma = 4.6$ and $Da_O = 10^4$ in Figure 6) and ultimately a system that behaves as a net source for nitrate. The net behavior can be explained by the large contribution of meander neck flow paths to the overall flux. In the following subsection, we explore a wide range of scenarios to better understand the controls on nitrogen retention/production within sinuosity-driven hyporheic zones.

3.2.1. Master Dimensionless Variables for Biogeochemical Potential: $\Pi_{C,c}$ and Da_O

We explore the overall hyporheic potential for biogeochemical transformations by exploring two master dimensionless variables that emerged from our dimensional analysis: (a) the availability of DOC relative to dissolved oxygen for water entering the hyporheic zone ($\Pi_{C,c} = C_{C,c}/C_{O,c}$) and (b) the Damköhler number for aerobic respiration ($Da_O = (V_O \lambda)/(K J_x)$). These variables are expected to play a fundamental role in nitrogen transformations and can be easily calculated at the catchment to continental scales from readily available hydrogeomorphic and empirical data. Note, however, that previous studies have almost exclusively focused on exploring the role of Da_O as a master variable for other hyporheic exchange processes (e.g., Gu et al., 2007;

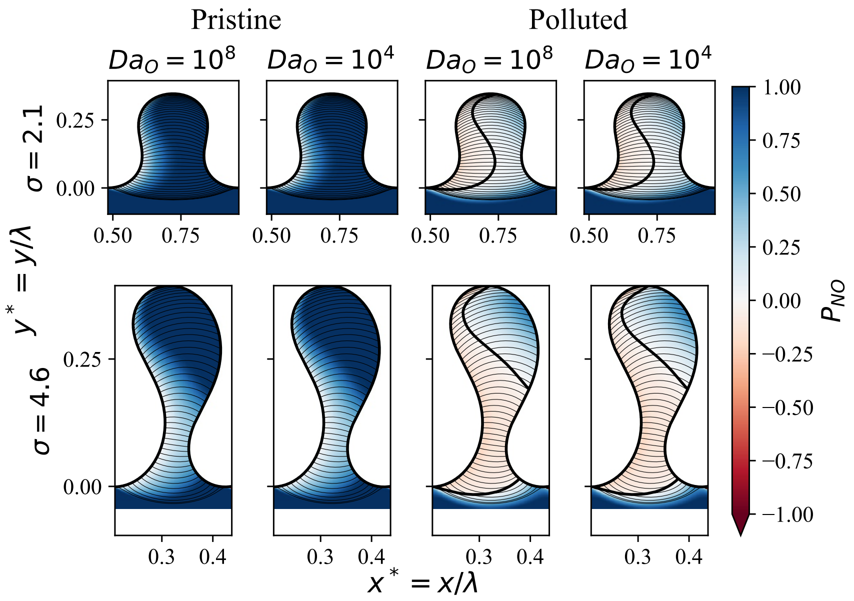

Figure 6. *Potential for the biogeochemical transformation of nitrate in a meander under neutral conditions* $(\Pi_{J_y} = 0)$ *with* $\Pi_{C,c} = 1$. The colors denote the potential P_{NO} (calculated with Equation 18), the thick black line denotes the zero contour value (transition from source to sink of nitrate), and the thin black lines denote streamlines. The two first columns show simulations for pristine conditions, while the last two show polluted conditions.

Zarnetske et al., 2012) without a systematic analysis of ΠC, c. This dimensionless ratio naturally emerges as a critical quantity from the scaling analysis, yet it is seldom considered a master variable. As we show here, $\Pi_{C,c}$ varies significantly in river networks and plays a significant role in the biogeochemical potential of sinuosity-driven hyporheic zones.

In the following, we summarize our results using the $\Pi_{C,c} - Da_O$ domain (Figure 7a), where each point represents a meander with different dimensionless variables, and therefore net biogeochemical potential (Figure 7b). This domain can be discretized into quadrants based on typical thresholds of the master variables. The first quadrant (upper left) is characterized by meanders with carbon ($\Pi_{C,c} < 1$) and transport ($Da_O > 1$) limitations. The second quadrant (lower left) is characterized by meanders with carbon ($\Pi_{C,c} < 1$) and reaction ($Da_O < 1$) limitations. The third quadrant (upper right) is characterized by meanders with oxygen ($\Pi_{C,c} > 1$) and transport ($Da_O > 1$) limitations. And lastly, the fourth quadrant (lower right) is characterized by meanders with oxygen ($\Pi_{C,c} > 1$) and reaction ($Da_O < 1$) limitations. From the MC analysis, which leverages hydrogeomorphic and chemical information across the conterminous United States (CONUS) (Section 2.2.2) and the literature values reported in Table 2, we estimated a subdomain of the $\Pi_{C,c} - Da_O$ domain where the CONUS meanders are more likely to map (see histograms and yellow rectangles in Figure 7a). However, their net behavior can change depending on the other dimensionless variables, especially the amount of particulate organic matter, which serves as a potential source of DOC to offset the carbon limitations (see, e.g., Sawyer, 2015).

Figure 7 illustrates a typical pattern of nitrate's biogeochemical potential (P_{NO}) for meanders in the $\Pi_{C,c} - Da_O$ domain. Using this figure as an example, we can discriminate meanders as sinks (blue colors) or sources (red colors) for nitrate. More specifically, reaction-limited ($Da_O < 1$) meanders tend to be mild sinks with $P_{NO} \gtrsim 0$. These meanders have characteristic time scales for reactant supply that are shorter than the time scales for reaction. In other words, the hyporheic zone does not provide enough time to consume oxygen, so denitrification is limited or has significant nitrification, which is equivalent to having a reactor where nitrate NO_3^- is transported without significant transformations. As Da_O exceeds unity, a source zone typically develops. This source zone eventually transitions to a strong sink zone as Da_O increases, where the transition threshold differs for carbon-limited ($\Pi_{C,c} < 1$) and oxygen-limited ($\Pi_{C,c} > 1$) systems. Oxygen-limited systems tend to transition after small values of Da_O, and, in some cases, the source zone does not develop. On the other hand, for carbon-limited systems, a large value of Da_O is needed before the system behaves as a nitrate sink.

19447973, 2024, 4, Downloaded from https://agupubs.onlinelibrary.wiley.com/doi/10.1029/2023WR036023, Wiley Online Library on [03/07/2024]. See the Terms and Conditions (https://onlinelibrary.wiley.com/terms-and-conditions) on Wiley Online Library for rules of use; OA articles are governed by the applicable Creative Commons License

19447973, 2024, 4, Downloaded from https://agupubs.onlinelibrary.wiley.com/doi/10.1029/2023WR036023, Wiley Online Library on [03/07/2024]. See the Terms and Conditions (https://onlinelibrary.wiley.com/terms-and-conditions) on Wiley Online Library for rules of use; OA articles are governed by the applicable Creative Commons License

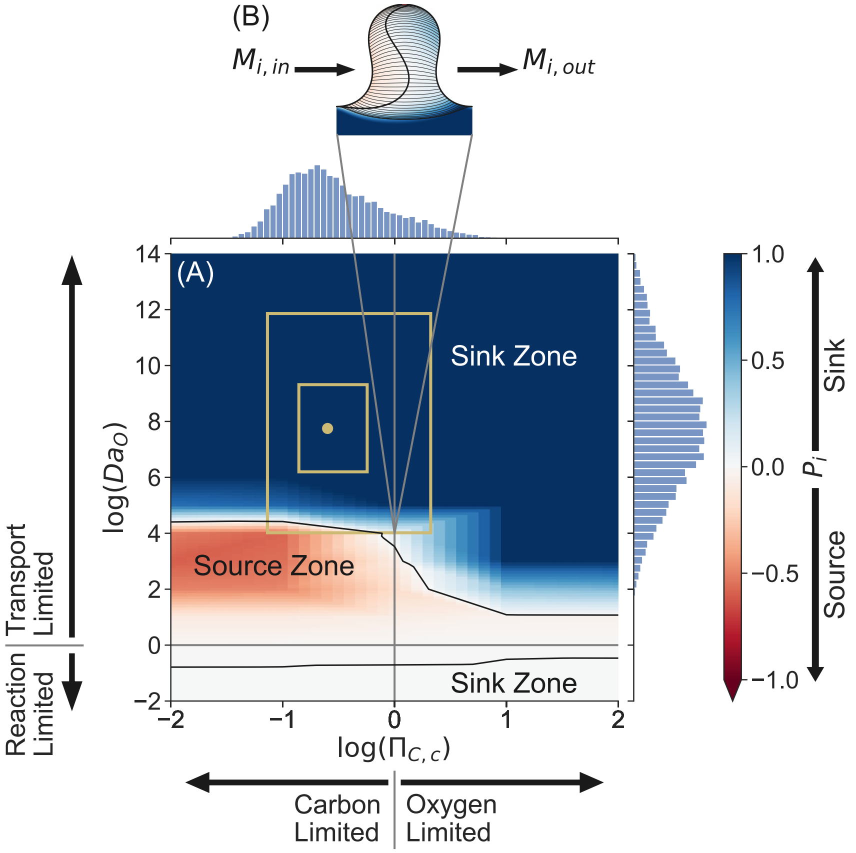

Figure 7. Biogeochemical potential in the $\Pi_{C,c} - Da_O$ domain (Panel a). Each point in this domain represents potential P_i for a single meander with dimensionless parameters $\Pi_{C,c}$ and Da_O (e.g., Panel b). The x-axis separates the domain into meanders exposed to carbon-limited ($\Pi_{C,c} < 1$) and oxygen-limited ($\Pi_{C,c} > 1$) boundary conditions, while the y-axis separates the domain into meanders characterized by reaction-limited ($Da_O < 1$) and transport-limited ($Da_O < 1$) conditions. For reference, we include histograms for typical values of the dimensionless variables found across the Conterminous US and their corresponding 5%, 25%, 50%, 75%, and 95% percentiles (yellow boxes and point). Generally, this diagram results in two characteristic zones: one for hyporheic zones that act as net sources of the constituent ($P_i < 0$; red colors) and one for meanders that act as net sinks ($P_i > 0$; blue colors).

To better understand the key controls on the $\Pi_{C,c} - Da_O$ zonation, we performed a systematic analysis for 800 meanders (i.e., scenarios) in pristine (low inorganic N) and polluted (high inorganic N) systems (L. Zheng et al., 2016) and with varying sinuosity, magnitudes of RGF, and availability of labile POC. First, we will focus on the effects of sinuosity and RGF for systems with a constant POC of 0.02%. Then, we will explore the implications of POC on the patterns observed.

3.2.1.1. Pristine Systems

Meanders in pristine systems (Figure 8; POC = 0.02%) are predominantly sinks for nitrate, with typical meanders across CONUS (yellow rectangles) having $P_{NO} \approx 1$. In some cases, small areas of the $\Pi_{C,c} - Da_O$ domain are classified as sources; however, P_{NO} is still close to zero, implying that these meanders behave as a net conveyor of nitrate with minimal transformations. In fact, systems with gaining conditions ($\Pi_{J_y} > 0$) do not develop a source zone.

The transition interface from mild to strong sink in the $\Pi_{C,c} - Da_O$ domain (transition from light to dark blue in Figure 8) is minimally affected by the magnitude of the RGF (i.e., similar patterns for all rows in a column). This transition, however, changes significantly with the degree of sinuosity. Systems with high FF transition to strong sinks at higher Da_O numbers, resulting in a larger proportion of CONUS meanders within the mild sink domain (area enclosed by the yellow rectangle). In other words, the likelihood of systems with conservative transport

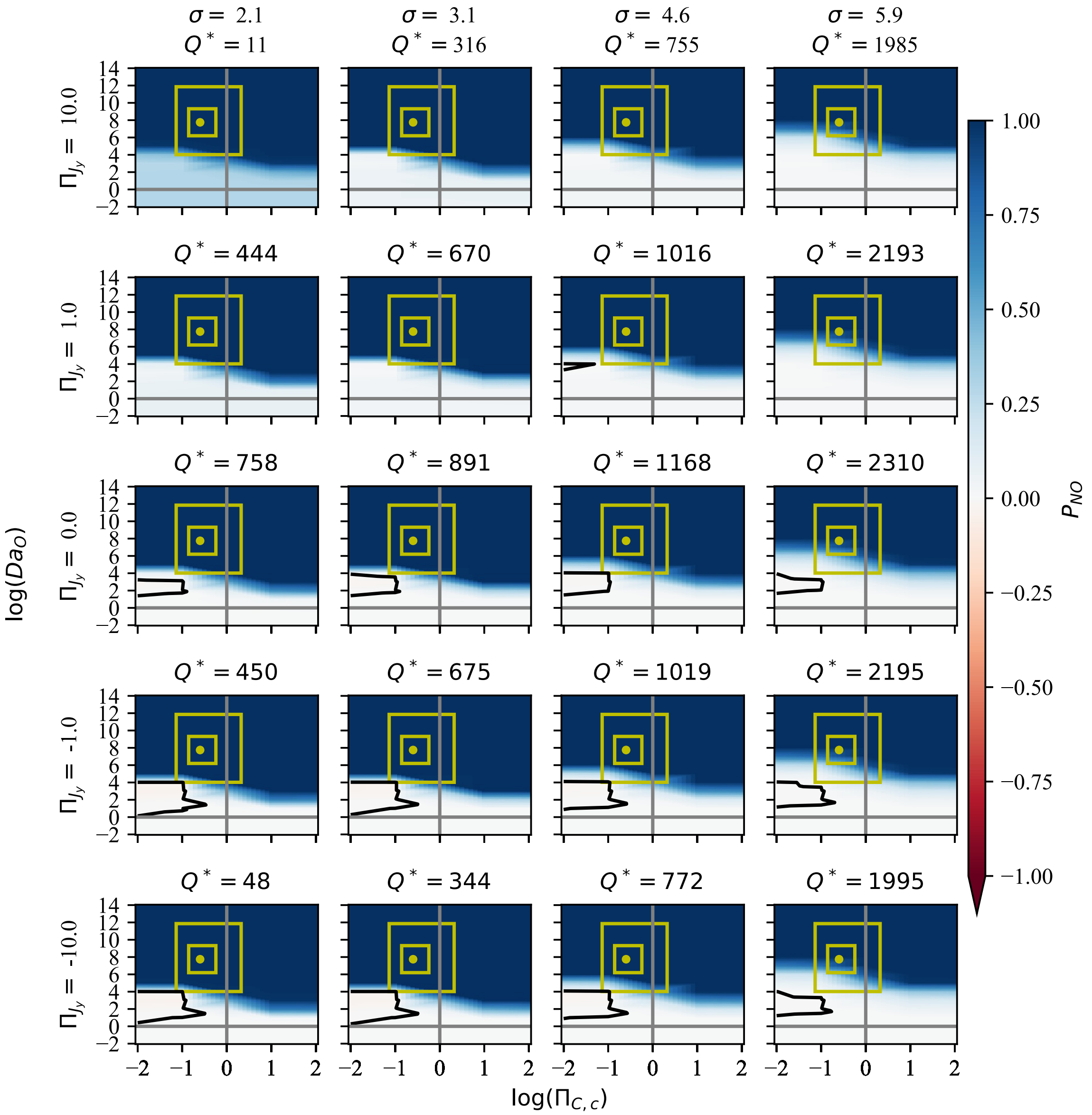

Figure 8. *Potential of retention of nitrates for the pristine river channel case and* $P_0 = 0.02\%$. The columns denote different meander topologies described by the sinuosity (σ). The rows separate the regional gradient Π_{J_y}. The colors show the potential for biogeochemical retention. The solid black line shows the zero contour line. The horizontal dashed line is the division between transport-limited ($\log(Da_O) > 0$) and reaction-limited systems ($\log(Da_O) < 0$). The vertical dashed lines is the division between carbon-limited ($\Pi_{C,c} < 0$) and oxygen-limited systems ($\Pi_{C,c} > 0$). For reference, we include histograms for typical values of the dimensionless variables found across the Conterminous US and their corresponding 5%, 25%, 50%, 75%, and 95% percentiles (yellow boxes and point).

behavior for NO_3^- increases with sinuosity. These findings are at odds with the common assumption that increasing sinuosity leads to increasing river corridor and hyporheic complexity and, therefore, a likely increase in river corridor biogeochemical processing—the basis for the design of typical hyporheic restoration efforts (Hester & Gooseff, 2010, 2011). Our model shows that the reduction of the net denitrification in high sinuosity meanders results from the higher velocities around the neck of the meander that transport a significant amount of water and solutes at higher rates, reducing the amount of time in contact with the reactive sediments for the majority of the flow. Based on the histograms derived for natural channels across CONUS (Figure 7), a predominant portion of channels will be sink zones in all cases for these conditions. As we show later, this transition can be highly sensitive to POC availability, completely changing the dynamics and overall behavior of these systems.

19447973, 2024, 4, Downloaded from https://agupubs.onlinelibrary.wiley.com/doi/10.1029/2023WR036023, Wiley Online Library on [03/07/2024]. See the Terms and Conditions (https://onlinelibrary.wiley.com/terms-and-conditions) on Wiley Online Library for rules of use; OA articles are governed by the applicable Creative Commons License

In general, a source zone of small extent and magnitude develops under neutral ($\Pi_{J_y} = 0$) and losing ($\Pi_{J_y} < 0$) RGF conditions. This zone is absent under gaining conditions ($\Pi_{J_y} > 0$). Under neutral conditions (third row in Figure 8), the source zone is smallest and roughly constrained to $\Pi_{C,c} \leq 10^{-1}$ and $10^2 \leq Da_O \leq 10^4$ and similar in shape for all sinuosity values. As the magnitude of the losing RGF increases, the source zone extends lower Da_O values, reaching $Da_O = 1$. As mentioned, the magnitude of the biogeochemical potential within the source zone is close to zero. We hypothesize that the expansion of the source zone under losing conditions is caused by dispersive mixing along the hyporheic zone boundary, which interacts with channel-born flow paths recharging the alluvial aquifer. The opposite effect is observed for gaining conditions given the boundary conditions assumed for the alluvial aquifer boundary in our model. In general, this dispersive mixing along the hyporheic zone boundary represents a minor fraction of the overall mass flowing through the hyporheic zone (Gomez et al., 2012; Hester & Gooseff, 2010, 2011; Hester et al., 2014).

The $\Pi_{C,c} - Da_O$ zonation for pristine systems is consistent with our expectations based on the microbial reaction process represented in our model. For these scenarios, the concentrations of NO_3^- and NH_4^+ at the channel (and their corresponding dimensionless variables $\Pi_{NO,c}$ and $\Pi_{NH,c}$) are relatively small. Low Da_O values characterize systems where meanders take longer to reach anoxic conditions, constraining denitrification, or the small amounts of NH_4^+ cannot drive significant nitrification. These conditions likely result in meanders that preferentially transport NO_3^- with negligible transformations. As Da_O increases, this oxic constraint becomes weaker, and preferentially anoxic conditions develop to facilitate denitrification. As shown in Figure 8, the development of these conditions occurs for lower Da_O values when DOC limitations are unimportant (i.e., $\Pi_{C,c} > 1$).

The effects of sinuosity can be explained by the dominant role of meander neck flow paths with shorter time scales. These flow paths move a larger proportion of total exchange as sinuosity increases. For example, oxic conditions extend a larger proportion of the meander neck due to shorter transport time scales, increasing the opportunities for nitrification while limiting denitrification. This effect explains the emergence of a source zone, which is mild due to the low supply of NH_4^+ that limits the production of NO_3^- through nitrification. As the sinuosity increases, and therefore the prevalence of short transport time scales characteristic of the meander neck, a higher Da_O value is needed to drive nitrification. This explains the upward migration of the strong sink transition in Figure 8.

3.2.1.2. Polluted Systems

Similar to L. Zheng et al. (2016), our polluted scenarios increase channel NO_3^- and NH_4^+ concentrations and their corresponding dimensionless variables by approximately one order of magnitude relative to pristine systems. Figure 9 illustrates the simulations in the $\Pi_{C,c} - Da_O$ domain with POC of 0.02%. The polluted scenarios are characterized by the emergence of a pronounced source zone that marks a transition from mild sinks, for low Da_O values, to strong sinks as Da_O increases. For the scenarios in this figure, a small fraction of probable value ranges for meanders across CONUS falls within the source zone. The lower boundary, marking the transition from mild sinks to strong sources, occurs at $Da_O = 1$ for neutral and gaining conditions; however, it can extend to $Da_O < 1$ for losing conditions. Note that the meanders with the lowest sinuosity and the strongest gaining conditions explored (upper left corner in Figure 9) present a different behavior, where the source zone is limited to a small region where $10^2 \leq Da_O \leq 10^4$ and $\Pi_{C,c} \leq 0.1$. As explained before, this difference is likely driven by mixing along the boundary of a highly compressed hyporheic zone.

The upper limit marking the transition from a strong source to strong sink meanders varies primarily as a function of sinuosity. For example, under neutral conditions, the transition boundary migrates toward higher Da_O values with increasing sinuosity. This is consistent with the dominant role of short residence times in higher sinuosity systems where neck flow paths dominate the total exchange flux. In this case, transport residence times constrain the capacity of the hyporheic zone to denitrify, resulting in a dominant role of nitrification that leads to a net source of nitrate. Furthermore, the zone is larger in carbon-limited systems ($\Pi_{C,c} < 1$), where aerobic respiration is likely consuming a large proportion of the available DOC, which limits the progression of denitrification. Nitrate source conditions can also be found for oxygen-limited systems, highlighting a "hot spot" of residence times where nitrification is favored (McClain et al., 2003; Zarnetske et al., 2011b). As it will be shown later, the dissolution of POC requires large enough Da_O to offset the DOC limitation and significantly activate the role of denitrification. This defines the location of the transition zone from source to sink as Da_O increases. Finally, as gaining fluxes increase ($\Pi_{J_y} > 0$), the source zone in the oxygen-limited quadrant disappears; this is consistent

19447973, 2024, 4, Downloaded from https://agupubs.onlinelibrary.wiley.com/doi/10.1029/2023WR036023, Wiley Online Library on [03/07/2024]. See the Terms and Conditions (https://onlinelibrary.wiley.com/terms-and-conditions) on Wiley Online Library for rules of use; OA articles are governed by the applicable Creative Commons License

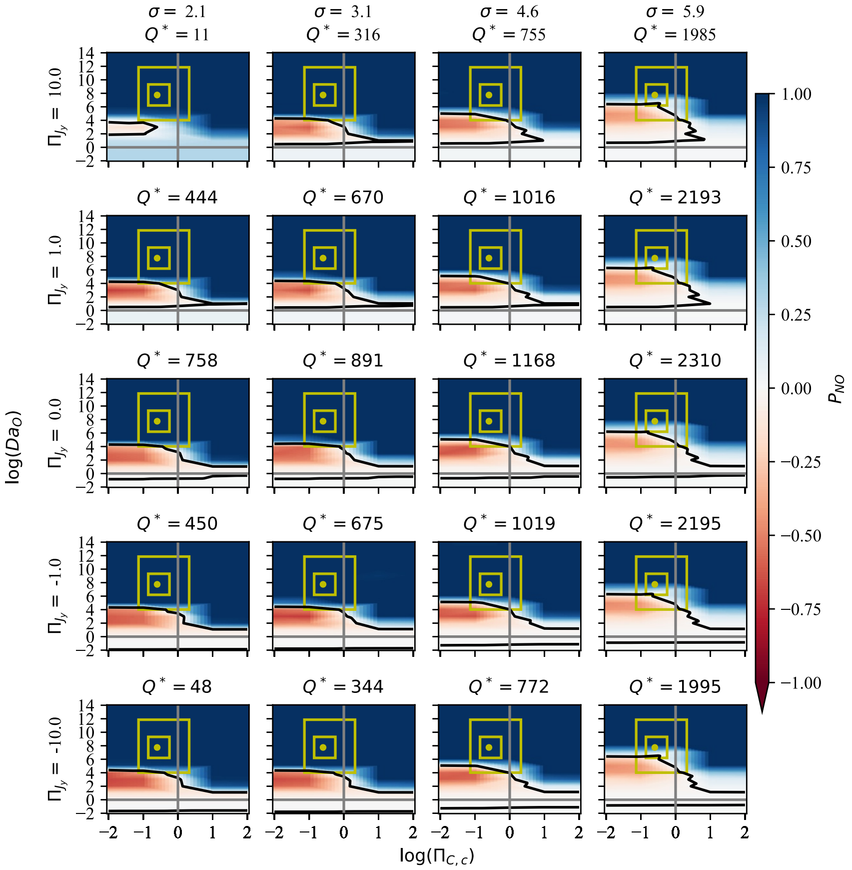

Figure 9. *Potential of retention of nitrates for the polluted river channel case and* $P_0 = 0.02\%$. The columns denote different meander topologies described by the sinuosity (σ). The rows separate the regional gradient Π_{J_y}. The colors show the potential for biogeochemical retention. The solid black line shows the zero contour line. The horizontal dashed line is the division between transport-limited ($\log(Da_O) > 0$) and reaction-limited systems ($\log(Da_O) < 0$). The vertical dashed lines is the division between carbon-limited ($\Pi_{C,c} < 0$) and oxygen-limited systems ($\Pi_{C,c} > 0$). For reference, we include histograms for typical values of the dimensionless variables found across the Conterminous US and their corresponding 5%, 25%, 50%, 75%, and 95% percentiles (yellow boxes and point).

with the removal of neck flow paths and a general increase in residence times, leading to enhancement of aerobic respiration and additional contact time under anoxic conditions, which ultimately enhances the role of denitrification. The net effect of these conditions is a transition to a net sink. This behavior is not consistent with losing conditions, given the mixing effects at the boundary of a thin hyporheic zone.

These findings have important implications for river restoration practices. If sinuosity is increased as a restoration strategy (e.g., Hester & Gooseff, 2010, 2011), the meander can act as a net source of nitrate, leading to adverse and unintended consequences from the perspective of nutrient retention. In fact, the overall negative impact increases with sinuosity, given that sinuosity significantly increases flux and, therefore, the overall contaminant load delivered from the hyporheic zone to the river. For example, the exchange increases by about two orders of magnitude when sinuosity is increased from 2.1 to 5.9 (Figure 9). As mentioned, this issue is driven by the dominant role of the meander neck as a control for the net flow and residence times within the meander's hyporheic zone.

3.2.2. The Role of Particulate Organic Carbon

Labile POC is a key constraint for offsetting DOC limitations in our simulations. The importance of this offset depends on the amount of POC available (represented by the dimensionless variable Π_{P-C}) and the dimensionless POC linear distribution coefficient (represented by Π_{Kd}). Here we illustrate the changes in the biogeochemical potential for NO_3^- transformations within the $\Pi_{C,c} - Da_O$ domain for three values of POC under pristine and

19447973, 2024, 4, Downloaded from https://agupubs.onlinelibrary.wiley.com/doi/10.1029/2023WR036023, Wiley Online Library on [03/07/2024]. See the Terms and Conditions (https://onlinelibrary.wiley.com/terms-and-conditions) on Wiley Online Library for rules of use; OA articles are governed by the applicable Creative Commons License

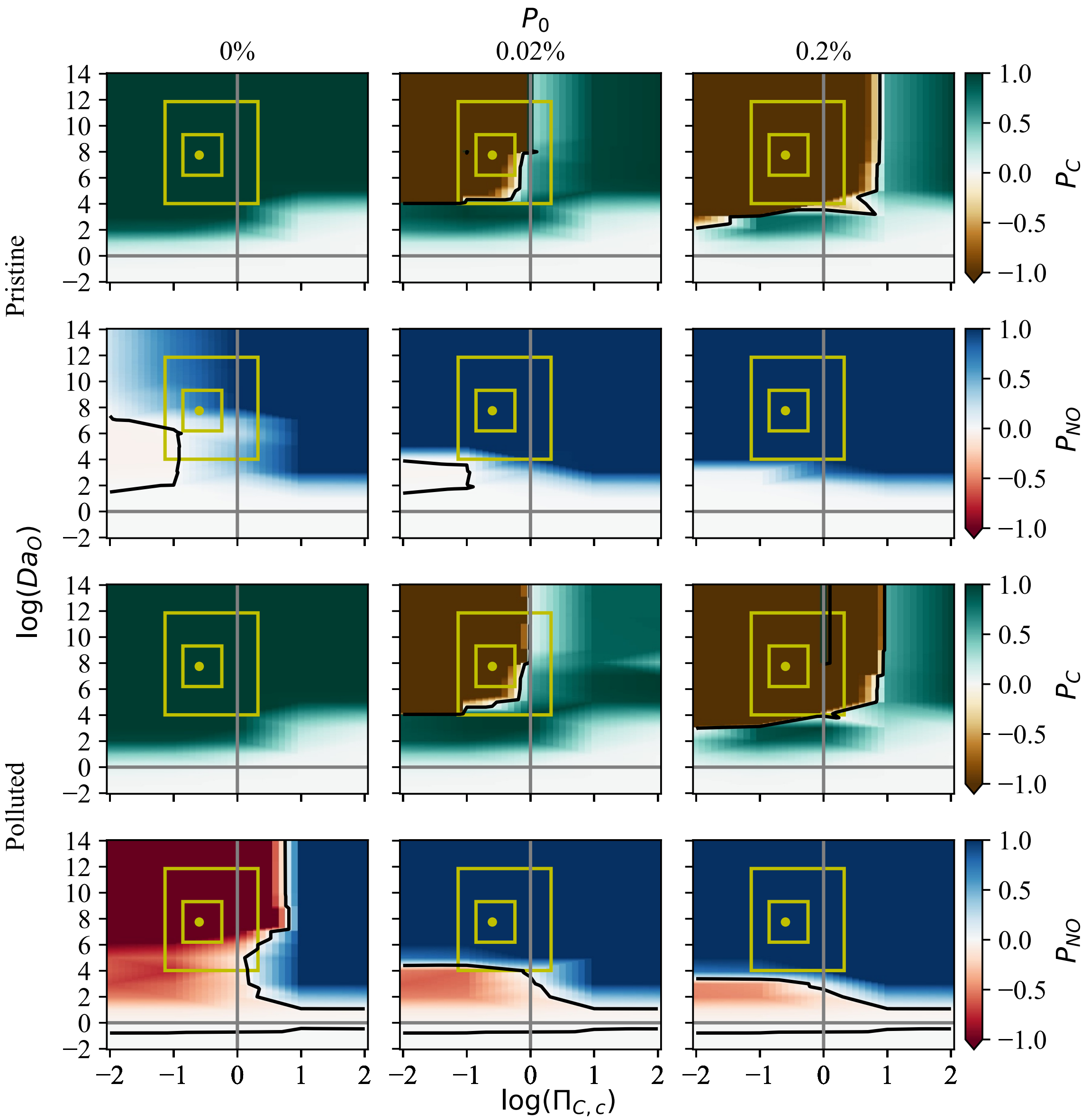

Figure 10. *Effect on particulate organic carbon (POC) concentration in the biogeochemical potential for dissolved organic carbon and* NO_3^- *transformations for meanders of moderate sinuosity* ($\sigma = 3.1$) *and neutral regional groundwater flow* ($\Pi_{J_y} = 0.0$). Columns correspond to labile POC of 0%, 0.02%, and 0.2%. The figure includes meanders under pristine (rows one and two) and polluted (rows three and four) channel conditions. The solid black line shows the zero contour line. The horizontal dashed line is the division between transport-limited ($\log(Da_O) > 0$) and reaction-limited systems ($\log(Da_O) < 0$). The vertical dashed lines is the division between carbon-limited ($\Pi_{C,c} < 0$) and oxygen-limited systems ($\Pi_{C,c} > 0$). For reference, we include histograms for typical values of the dimensionless variables found across the Conterminous US and their corresponding 5%, 25%, 50%, 75%, and 95% percentiles (yellow boxes and point).

contaminated conditions. These results are summarized in Figure 10 for a single meander ($\sigma = 3.1$) under neutral conditions. Note that the role of Π_{Kd} decreases as POC increases (see Supporting Information S1 for additional details), and therefore, we focus on Π_{P-C}, which is directly proportional to POC.

The systems without POC available to offset DOC limitations (first column of Figure 10) consume all the DOC available through aerobic respiration, which in turn constrains the role of denitrification because it needs DOC to proceed. When aerobic respiration is limited by the availability of DOC or short transport time scales, the oxygen remaining can promote nitrification and lead to the formation of a nitrate source zone (red areas in the $\Pi_{C,c} - Da_O$ domain). The nitrification reaction is then limited by the availability of NH_4^+. In the case of the polluted river channels, the nitrate source zone is constrained to $\Pi_{C,c} \leq 0.1$ and $10^2 \leq Da_O \geq 10^7$. For polluted channels, the

19447973, 2024, 4, Downloaded from https://agupubs.onlinelibrary.wiley.com/doi/10.1029/2023WR036023, Wiley Online Library on [03/07/2024]. See the Terms and Conditions (https://onlinelibrary.wiley.com/terms-and-conditions) on Wiley Online Library for rules of use; OA articles are governed by the applicable Creative Commons License

nitrate source zone extends the majority of the carbon-limited domain and some sections of the oxygen-limited domain, primarily for small Da_O values. The meanders from the CONUS analysis (yellow rectangles) will be within the source zone under polluted conditions, imposing a positive feedback cycle where the sinuosity-driven hyporheic zone may exacerbate the nitrate excess problems.

As the available POC increases to 0.002% and 0.2%, we see the emergence of a strong source zone for DOC (dark brown colors with $P_C < 0$). The DOC promotes aerobic respiration and denitrification while suppressing nitrification. In other words, the overall effect of the dissolution of POC is to compress the nitrate source zone in the $\Pi_{C,c} - Da_O$ domain and to expand the zones classified as strong sinks. This effect is particularly important in polluted systems where the CONUS meanders transition to sinks of nitrate with POC concentrations as small as 0.02%. Note, however, that the increases in POC do not completely eliminate the nitrate source zone, but it significantly decreases its extent. Hence, the availability and reactivity of organic carbon are likely a significant control on the fate of the nitrogen in meanders, and the reactivity of DOC remains an understudied area of field hyporheic research (Zarnetske et al., 2012).

4. Conclusions

Meanders in river channels provide a critical and underappreciated natural biogeochemical reactor. Our models and simulations provide a fundamental understanding of the role that first-order drivers (meander topology) and modulators (RGF) play in the hydrodynamics, transport, and reactions taking place within sinuosity-driven hyporheic zones occurring in meanders. Furthermore, we reveal and propose a dimensionless framework to characterize these processes in terms of metrics that can be quantified by widely available remote sensing and water quality data. These metrics, at the same time, offer a first step toward the development of a new generation of surrogate models that explicitly include the role of meanders in water quality modeling efforts.

From the perspective of the hyporheic exchange hydrodynamics, meander topology, and in particular, the relative size of the meander neck (expressed as a FF), emerges as a key variable controlling the total amount of exchange and the characteristic time scales for transport. As sinuosity increases, the FF increases, leading to a hydrodynamic shielding effect that protects the sinuosity-driven hyporheic zone from the compressing effects of RGF. This effect highlights the robust nature of this hyporheic exchange process along river corridors and shows that it can be more important and ubiquitous than previously thought (Cardenas, 2009a, 2009b; Gomez et al., 2012; Gomez-Velez et al., 2015, 2017).

Meander topology also plays a key control in multiple biogeochemical transformations taking place within the hyporheic zone. Here, we focused on nitrogen transformation, and in particular on the fate of nitrate. However, other transformations of interest could be explored within a similar framework, especially those chemical transformations associated with oxidation-reduction (redox) processes and carbon utilization (e.g., Burgin & Loecke, 2023; Hedin et al., 1998). Our simulations show the complex interplay between transport and biogeochemical time scales, substrate availability, and sinuosity. Topology and RGF determine the transport time scales, solute concentrations at the channel impose critical boundary conditions and limitations, alluvial aquifer biogeochemical parameters impose transformation time scales, and availability of POC becomes a critical factor to offset carbon limitations. All these factors can lead to similar meanders acting as net sources or sinks of nitrate. Understanding their role allows us to predict the potential implications of the exchange process and propose reasonable restoration strategies that take advantage of the natural potential of river corridors to remove excess nitrogen (e.g., Hester & Gooseff, 2010, 2011). For example, a practitioner interested in increasing sinuosity for channel restoration purposes could use field measurements and estimates of the expected post-restoration sinuosity to map scenarios into the $\Pi_{C,c} - Da_o$ domain (Figures 8–10). This mapping would provide a "back-of-the-envelope" prediction for the expected behavior of the meanders under the proposed restoration strategy. More generally, this framework offers general insight into the tight coupling of substrate availability, residence times, and channel topology.

Although our conceptual model is idealized, we are confident it captures the first-order controls for the exchange process, providing fundamental insight into the biogeochemical potential of meanders across river corridors. Furthermore, it provides a scalable framework to explore multiple meander topologies and regional groundwater conditions. Finally, our results stress the vital role of dissolved and POC content in the biogeochemical potential of sinuosity-driven hyporheic zones and, in particular, the need to better constrain POC content in stream sediments and alluvial aquifers.

19447973, 2024, 4, Downloaded from https://agupubs.onlinelibrary.wiley.com/doi/10.1029/2023WR036023, Wiley Online Library on [03/07/2024]. See the Terms and Conditions (https://onlinelibrary.wiley.com/terms-and-conditions) on Wiley Online Library for rules of use; OA articles are governed by the applicable Creative Commons License

19447973, 2024, 4, Downloaded from https://agupubs.onlinelibrary.wiley.com/doi/10.1029/2023WR036023, Wiley Online Library on [03/07/2024]. See the Terms and Conditions (https://onlinelibrary.wiley.com/terms-and-conditions) on Wiley Online Library for rules of use; OA articles are governed by the applicable Creative Commons License

It is important to note that the assumptions behind the reduced-complexity model carry important limitations, most of which can be relaxed in future applications. First, our model neglects the three-dimensional nature of groundwater flow and the nested nature of exchange processes. This three-dimensional structure can be particularly important near the channel (e.g., Boano, Camporeale, & Revelli, 2010; Boano et al., 2014; Perez et al., 2021; Stonedahl et al., 2013; Wang et al., 2022), where convergent flow and the interplay of multiple morphologies driving hyporheic exchange are a first-order control for transport and reaction. Second, we assume a homogeneous and isotropic porous media, ignoring the important role of physical and biogeochemical heterogeneity (e.g., Arora et al., 2022; Song et al., 2020; Zhou et al., 2014), which plays a central role in the formation of biogeochemical hotspots (e.g., Briggs et al., 2018; Krause et al., 2022). The representation of POC heterogeneity (Sawyer, 2015) and its liability (J. Zheng et al., 2019) is of particular interest, which is ignored in the current conceptualization. Lastly, we assume a steady river stage and constituent concentration. As mentioned before, these boundary conditions covary over space and time (Creed et al., 2015), constraining exchange dynamics, residence times, and substrate supply (e.g., Dwivedi et al., 2018; Gomez-Velez et al., 2017; Song et al., 2020; Wu et al., 2021). Future work should consider the temporal dynamics and correlations of discharge and concentrations (e.g., Dwivedi et al., 2018; Gomez-Velez et al., 2017), the influence of heterogeneity in sediments (e.g., Sawyer, 2015), and the potential implications of including our conceptualization into reach-scale water quality models, where the effects of concentrations on reaction rates play a significant role (e.g., Schmadel et al., 2020).

Notation

θ	Kinoshita angle [–]
s	Streamwise coordinate [L]
θ_0	Maximum angular amplitude [–]
λ	Arc wavelength [L]
J_s	Skewness coefficient [–]
J_f	Flatness coefficient [–]
x	Spatial coordinate vector [L]
Q	Vertical integrated flux [L^2T^{-1}]
Q*	Dimensionless vertical integrated flux [–]
Q	Darcy flux [LT^{-1}]
K	Hydraulic conductivity [LT^{-1}]
H	Saturated thickness [L]
h	Hydraulic head [L]
h^*	Dimensionless hydraulic head [–]
Z_b	Vertical location of impermeable layer [L]
J_x	Average valley slope (x-direction) [–]
J_y	Average slope of the far-field water table (y-direction) [–]
L	Meander wavelength parallel to the alluvial valley [L]
H_c	Channel saturated thickness [L]
σ	Sinuosity [–]
Π_{H_c}	Dimensionless channel number [–]
Π_{J_y}	Dimensionless slope ratio number [–]
ψ	Water age distribution [T^{-1}]

Ψ	Cumulative age distribution [–]
τ	Water age [T]
τ_v	Mean water age [T]
ϵ_p	Porosity [–]
D	Vertically integrated dispersion-diffusion tensor [L^3T^{-1}]
α_T	Transverse dispersivity [L]
α_L	Longitudinal dispersivity [L]
$\delta_{i,j}$	Kronecker delta function [–]
η	Tortuosity factor [–]
D_m	Molecular diffusion [L^2T^{-1}]
τ_c	Characteristic time scale [T^{-1}]
C_i	Concentration of chemical constituent i [ML^{-3}]
R_i	Reaction rates of chemical constituent i [$ML^{-3}T^{-1}$]
V_i	Maximum microbial process reaction rate for chemical constituent i [T^{-1}]
X_j	Biomass of the jth functional microbial group [ML^{-3}]
K_I	Inhibition constant for denitrification reaction [ML^{-3}]
K_i	Half-saturation constant [ML^{-3}]
y_i	Partition coefficient [–]
ρ_b	Bulk density [ML^{-3}]
P	Particulate organic carbon ($MM^{-1}_{\text{sediment}}$)
α	First-order mass transfer coefficient [T^{-1}]
K_d	Linear distribution coefficient for the sediment ($L^3M^{-1}_{sediment}$)
Da_i	Damköhler number of chemical constituent i [–]
$\Pi_{C_{i,c}}$	Dimensionless concentration of the channel for chemical constituent i [–]
$\Pi_{C_{i,v}}$	Dimensionless concentration of the valley for chemical constituent i [–]
Π_{K_i}	Dimensionless half-saturation coefficient for chemical constituent i [–]
Π_{K_I}	Dimensionless inhibition coefficient [–]
Π_{K_d}	Dimensionless particulate organic carbon linear distribution coefficient [–]
FF	Funneling factor [–]
L_n	Maximum distance within the meander neck [–]
L_l	Maximum distance within the meander lobe [–]
P_i	Net biogeochemical potential of chemical constituent i [–]
M_i	Mass of chemical constituent i [–]

19447973, 2024, 4, Downloaded from https://agupubs.onlinelibrary.wiley.com/doi/10.1029/2023WR036023, Wiley Online Library on [03/07/2024]. See the Terms and Conditions (https://onlinelibrary.wiley.com/terms-and-conditions) on Wiley Online Library for rules of use; OA articles are governed by the applicable Creative Commons License

19447973, 2024, 4, Downloaded from https://agupubs.onlinelibrary.wiley.com/doi/10.1029/2023WR036023, Wiley Online Library on [03/07/2024]. See the Terms and Conditions (https://onlinelibrary.wiley.com/terms-and-conditions) on Wiley Online Library for rules of use; OA articles are governed by the applicable Creative Commons License

Data Availability Statement

The data and Python scripts needed to reproduce the analyses and figures in this study are available through Gonzalez-Duque et al. (2024).

Acknowledgments

This research was funded by the U.S. Department of Energy (DOE), Office of Science, Biological and Environmental Research. This work is a product of two programs: (a) Environmental System Science Program, as part of the River Corridor Scientific Focus Area project at Pacific Northwest National Laboratory, the Watershed Dynamics and Evolution Science Focus Area at Oak Ridge National Laboratory, and the IDEAS-Watersheds project, and (b) Data Management Program, as part of the ExaSheds project. Additional support was provided by the National Science Foundation (awards EAR-1830172, OIA-2020814, and OIA-2312326). This manuscript has been co-authored by staff from UT-Battelle, LLC, under contract DE-AC05-00OR22725 with the US Department of Energy (DOE). The US government retains and the publisher, by accepting the article for publication, acknowledges that the US government retains a nonexclusive, paid-up, irrevocable, worldwide license to publish or reproduce the published form of this manuscript, or allow others to do so, for US government purposes. DOE will provide public access to these results of federally sponsored research in accordance with the DOE Public Access Plan (http://energy.gov/downloads/doe-public-access-plan).

References

Abad, J. D., & Garcia, M. H. (2009). Experiments in a high-amplitude Kinoshita meandering channel: 1. Implications of bend orientation on mean and turbulent flow structure. *Water Resources Research*, *45*(2), W02401. https://doi.org/10.1029/2008WR007016

Anderson, R. S., & Anderson, S. P. (2010). *Geomorphology: The mechanics and chemistry of landscapes*. Cambridge University Press.

Arora, B., Briggs, M. A., Zarnetske, J. P., Stegen, J., Gomez-Velez, J. D., Dwivedi, D., & Steefel, C. (2022). Hot spots and hot moments in the critical zone: Identification of and incorporation into reactive transport models. In A. S. Wymore, W. H. Yang, W. L. Silver, W. H. McDowell, & J. Chorover (Eds.), *Biogeochemistry of the critical zone* (pp. 9–47). Springer International Publishing. https://doi.org/10.1007/978-3-030-95921-0_2

Arrigoni, A. S., Poole, G. C., Mertes, L. A. K., O'Daniel, S. J., Woessner, W. W., & Thomas, S. A. (2008). Buffered, lagged, or cooled? Disentangling hyporheic influences on temperature cycles in stream channels. *Water Resources Research*, *44*(9), W09418. https://doi.org/10.1029/2007WR006480

Baker, M., Dahm, C., & Valett, H. (1999). Acetate retention and metabolism in the hyporheic zone of a mountain stream. *Limnology and Oceanography*, *44*(6), 1530–1539. https://doi.org/10.4319/lo.1999.44.6.1530

Bear, J. (1972). *Dynamics of fluids in porous media*. American Elsevier Publishing.

Bear, J., & Cheng, A. H.-D. (2010). *Modeling groundwater flow and contaminant transport* (1st ed.). Springer Netherlands. (No. 23).

Bekins, B. A., Warren, E., & Godsy, E. M. (1998). A Comparison of zero-order, first-order, and Monod biotransformation models. *Groundwater*, *36*(2), 261–268. https://doi.org/10.1111/j.1745-6584.1998.tb01091.x

Bencala, K. E. (2011). 2.20 - Stream–groundwater interactions. In P. Wilderer (Ed.), *Treatise on water science* (pp. 537–546). Elsevier. https://doi.org/10.1016/B978-0-444-53199-5.00115-9

Boano, F., Camporeale, C., & Revelli, R. (2010). A linear model for the coupled surface-subsurface flow in a meandering stream. *Water Resources Research*, *46*(7), 14. https://doi.org/10.1029/2009WR008317

Boano, F., Camporeale, C., Revelli, R., & Ridolfi, L. (2006). Sinuosity-driven hyporheic exchange in meandering rivers. *Geophysical Research Letters*, *33*(18), L18406. https://doi.org/10.1029/2006GL027630

Boano, F., Demaria, A., Revelli, R., & Ridolfi, L. (2010). Biogeochemical zonation due to intrameander hyporheic flow. *Water Resources Research*, *46*(2). https://doi.org/10.1029/2008WR007583

Boano, F., Harvey, J. W., Marion, A., Packman, A. I., Revelli, R., Ridolfi, L., & Wörman, A. (2014). Hyporheic flow and transport processes: Mechanisms, models, and biogeochemical implications. *Reviews of Geophysics*, *52*(4), 603–679. https://doi.org/10.1002/2012RG000417

Briggs, M. A., Day-Lewis, F. D., Dehkordy, F. M. P., Hampton, T., Zarnetske, J. P., Scruggs, C. R., et al. (2018). Direct observations of hydrologic exchange occurring with less-mobile porosity and the development of anoxic microzones in sandy lakebed sediments. *Water Resources Research*, *54*(7), 4714–4729. https://doi.org/10.1029/2018WR022823

Buffington, J. M., Montgomery, D. R., & Greenberg, H. M. (2004). Basin-scale availability of salmonid spawning gravel as influenced by channel type and hydraulic roughness in mountain catchments. *Canadian Journal of Fisheries and Aquatic Sciences*, *61*(11), 2085–2096. https://doi.org/10.1139/f04-141

Buffington, J. M., & Tonina, D. (2009). Hyporheic exchange in mountain rivers II: Effects of channel morphology on mechanics, scales, and rates of exchange: Channel morphology and hyporheic exchange. *Geography Compass*, *3*(3), 1038–1062. https://doi.org/10.1111/j.1749-8198.2009.00225.x

Burgin, A. J., & Loecke, T. D. (2023). The biogeochemical redox paradox: How can we make a foundational concept more predictive of biogeochemical state changes? *Biogeochemistry*, *164*(2), 349–370. https://doi.org/10.1007/s10533-023-01036-9

Camporeale, C., Perona, P., Porporato, A., & Ridolfi, L. (2007). Hierarchy of models for meandering rivers and related morphodynamic processes. *Reviews of Geophysics*, *45*(1), RG1001. https://doi.org/10.1029/2005RG000185

Cardenas, M. B. (2008). The effect of river bend morphology on flow and timescales of surface water–groundwater exchange across pointbars. *Journal of Hydrology*, *362*(1–2), 134–141. https://doi.org/10.1016/j.jhydrol.2008.08.018

Cardenas, M. B. (2009a). A model for lateral hyporheic flow based on valley slope and channel sinuosity. *Water Resources Research*, *45*(1), W01501. https://doi.org/10.1029/2008WR007442

Cardenas, M. B. (2009b). Stream-aquifer interactions and hyporheic exchange in gaining and losing sinuous streams. *Water Resources Research*, *45*(6), W06429. https://doi.org/10.1029/2008WR007651

COMSOL AB. (2024). COMSOL Multiphysics®. [Software]. Retrieved from https://www.comsol.com/

Creed, I. F., McKnight, D. M., Pellerin, B. A., Green, M. B., Bergamaschi, B. A., Aiken, G. R., et al. (2015). The river as a chemostat: Fresh perspectives on dissolved organic matter flowing down the river continuum. *Canadian Journal of Fisheries and Aquatic Sciences*, *72*(8), 1272–1285. https://doi.org/10.1139/cjfas-2014-0400

Dahm, C., Grimm, N., Marmonier, P., Valett, H., & Vervier, P. (1998). Nutrient dynamics at the interface between surface waters and groundwaters. *Freshwater Biology*, *40*(3), 427–451. https://doi.org/10.1046/j.1365-2427.1998.00367.x

Deng, F., Hou, L., Liu, M., Zheng, Y., Yin, G., Li, X., et al. (2015). Dissimilatory nitrate reduction processes and associated contribution to nitrogen removal in sediments of the Yangtze Estuary. *Journal of Geophysical Research: Biogeosciences*, *120*(8), 1521–1531. https://doi.org/10.1002/2015JG003007

Dent, C. L., Grimm, N. B., & Fisher, S. G. (2001). Multiscale effects of surface–subsurface exchange on stream water nutrient concentrations. *Journal of the North American Benthological Society*, *20*(2), 162–181. https://doi.org/10.2307/1468313

Dent, C. L., Schade, J. D., Grimm, N. B., & Fisher, S. G. (2000). 16 - Subsurface influences on surface biology. In J. B. Jones & P. J. Mulholland (Eds.), *Streams and ground waters* (pp. 381–402). Academic Press. https://doi.org/10.1016/B978-012389845-6/50017-X

Diamond, J. S., Pinay, G., Bernal, S., Cohen, M. J., Lewis, D., Lupon, A., et al. (2023). Light and hydrologic connectivity drive dissolved oxygen synchrony in stream networks. *Limnology and Oceanography*, *68*(2), 322–335. https://doi.org/10.1002/lno.12271

Dodds, W. K., Perkin, J. S., & Gerken, J. E. (2013). Human impact on freshwater ecosystem services: A global perspective. *Environmental Science & Technology*, *47*(16), 9061–9068. https://doi.org/10.1021/es4021052

Dwivedi, D., Arora, B., Steefel, C. I., Dafflon, B., & Versteeg, R. (2018). Hot spots and hot moments of nitrogen in a riparian corridor. *Water Resources Research*, *54*(1), 205–222. https://doi.org/10.1002/2017WR022346

Ginn, T. (1999). On the distribution of multicomponent mixtures over generalized exposure time in subsurface flow and reactive transport: Foundations, and formulations for groundwater age, chemical heterogeneity, and biodegradation. *Water Resources Research*, *35*(5), 1395–1407. https://doi.org/10.1029/1999wr900013

Gomez, J. D., & Wilson, J. L. (2013). Age distributions and dynamically changing hydrologic systems: Exploring topography-driven flow. *Water Resources Research*, *49*(3), 1503–1522. https://doi.org/10.1002/wrcr.20127

Gomez, J. D., Wilson, J. L., & Cardenas, M. B. (2012). Residence time distributions in sinuosity-driven hyporheic zones and their biogeochemical effects: RTD in hyporheic zones and biogeochemical effects. *Water Resources Research*, *48*(9), 9533. https://doi.org/10.1029/2012WR012180

Gomez-Velez, J. D., & Harvey, J. W. (2014). A hydrogeomorphic river network model predicts where and why hyporheic exchange is important in large basins. *Geophysical Research Letters*, *41*(18), 6403–6412. https://doi.org/10.1002/2014GL061099

Gomez-Velez, J. D., Harvey, J. W., Cardenas, M. B., & Kiel, B. (2015). Denitrification in the Mississippi River network controlled by flow through river bedforms. *Nature Geoscience*, *8*(12), 941–945. https://doi.org/10.1038/ngeo2567

Gomez-Velez, J. D., Krause, S., & Wilson, J. L. (2014). Effect of low-permeability layers on spatial patterns of hyporheic exchange and groundwater upwelling. *Water Resources Research*, *50*(6), 5196–5215. https://doi.org/10.1002/2013WR015054

Gomez-Velez, J. D., Wilson, J. L., Cardenas, M. B., & Harvey, J. W. (2017). Flow and residence times of dynamic river bank storage and sinuosity-driven hyporheic exchange: Bank storage and hyporheic exchange. *Water Resources Research*, *53*(10), 8572–8595. https://doi.org/10.1002/2017WR021362

Gonzalez-Duque, D., Gomez-Velez, J. D., Zarnetske, J. P., Chen, X., & Scheibe, T. D. (2024). Scripts for: “Sinuosity-driven Hyporheic Exchange: Hydrodynamics and Biogeochemical Potential” [Software]. FigShare. https://doi.org/10.6084/m9.figshare.23881518

Gothäll, H. (2022). How to inspect your mesh in COMSOL Multiphysics®. Retrieved from https://www.comsol.com/blogs/how-to-inspect-your-mesh-in-comsol-multiphysics/

Green, C. T., Liao, L., Nolan, B. T., Juckem, P. F., Shope, C. L., Tesoriero, A. J., & Jurgens, B. C. (2018). Regional variability of nitrate fluxes in the unsaturated zone and groundwater, Wisconsin, USA. *Water Resources Research*, *54*(1), 301–322. https://doi.org/10.1002/2017WR022012

Gu, C., Anderson, W., & Maggi, F. (2012). Riparian biogeochemical hot moments induced by stream fluctuations. *Water Resources Research*, *48*(9), W09546. https://doi.org/10.1029/2011WR011720

Gu, C., Hornberger, G. M., Herman, J. S., & Mills, A. L. (2008a). Effect of freshets on the flux of groundwater nitrate through streambed sediments. *Water Resources Research*, *44*(5), 12. https://doi.org/10.1029/2007WR006488

Gu, C., Hornberger, G. M., Herman, J. S., & Mills, A. L. (2008b). Influence of stream-groundwater interactions in the streambed sediments on NO_3-flux to a low-relief coastal stream. *Water Resources Research*, *44*(11), W11432. https://doi.org/10.1029/2007WR006739

Gu, C., Hornberger, G. M., Mills, A. L., Herman, J. S., & Flewelling, S. A. (2007). Nitrate reduction in streambed sediments: Effects of flow and biogeochemical kinetics. *Water Resources Research*, *43*(12), W12413. https://doi.org/10.1029/2007WR006027

Hancock, P. J. (2002). Human impacts on the stream-groundwater exchange zone. *Environmental Management*, *29*(6), 763–781. https://doi.org/10.1007/s00267-001-0064-5

Harvey, J. W., Gomez-Velez, J., Schmadel, N., Scott, D., Boyer, E., Alexander, R., et al. (2018). How hydrologic connectivity regulates water quality in river corridors. *JAWRA Journal of the American Water Resources Association*, *55*(2), 369–381. https://doi.org/10.1111/1752-1688.12691

Harvey, J. W., & Gooseff, M. (2015). River corridor science: Hydrologic exchange and ecological consequences from bedforms to basins. *Water Resources Research*, *51*(9), 6893–6922. https://doi.org/10.1002/2015WR017617

Harvey, J. W., & Schmadel, N. M. (2021). The river corridor's evolving connectivity of lotic and lentic waters. *Frontiers in Water*, *2*, 580727. https://doi.org/10.3389/frwa.2020.580727

Hedin, L. O., von Fischer, J. C., Ostrom, N. E., Kennedy, B. P., Brown, M. G., & Robertson, G. P. (1998). Thermodynamic constraints on nitrogen transformations and other biogeochemical processes at soil-stream interfaces. *Ecology*, *79*(2), 684–703. https://doi.org/10.2307/176963

Hester, E. T., & Gooseff, M. (2010). Moving beyond the banks: Hyporheic restoration is fundamental to restoring ecological services and functions of streams. *Environmental Science & Technology*, *44*(5), 1521–1525. https://doi.org/10.1021/es902988n

Hester, E. T., & Gooseff, M. N. (2011). Hyporheic restoration in streams and rivers. In A. Simon, B. Bennett, & J. Castro (Eds.), *Stream restoration in dynamic fluvial systems: Scientific approaches, analyses, and tools* (Vol. 194, pp. 167–187). American Geophysical Union.

Hester, E. T., Young, K. I., & Widdowson, M. A. (2014). Controls on mixing-dependent denitrification in hyporheic zones induced by riverbed dunes: A steady state modeling study. *Water Resources Research*, *50*(11), 9048–9066. https://doi.org/10.1002/2014WR015424

Hill, R. A., Weber, M. H., Leibowitz, S. G., Olsen, A. R., & Thornbrugh, D. J. (2016). The Stream-Catchment (StreamCat) dataset: A database of watershed metrics for the conterminous United States. *JAWRA Journal of the American Water Resources Association*, *52*(1), 120–128. https://doi.org/10.1111/1752-1688.12372

Holmes, R. (2000). The importance of ground water to stream ecosystem function. In J. B. Jones & P. J. Mulholland (Eds.), *Streams and ground waters* (pp. 137–148). https://doi.org/10.1016/B978-012389845-6/50006-5

Hunter, K., Wang, Y., & Van Cappellen, P. (1998). Kinetic modeling of microbially-driven redox chemistry of subsurface environments: Coupling transport, microbial metabolism and geochemistry. *Journal of Hydrology*, *209*(1), 53–80. https://doi.org/10.1016/s0022-1694(98)00157-7

Jardine, P. M., Dunnivant, F. M., McCarthy, J. F., & Selim, H. M. (1992). Comparison of models for describing the transport of dissolved organic carbon in aquifer columns. *Soil Science Society of America Journal*, *56*(2), 393–401. https://doi.org/10.2136/sssaj1992.03615995005600020009x

Kiel, B. A., & Bayani Cardenas, M. (2014). Lateral hyporheic exchange throughout the Mississippi River network. *Nature Geoscience*, *7*(6), 413–417. https://doi.org/10.1038/ngeo2157

Kinoshita, R., & Miwa, H. (1974). River channel formation which prevents downstream translation of transverse bars. *ShinSabo*, *94*, 12–17.

Krause, S., Abbott, B. W., Baranov, V., Bernal, S., Blaen, P., Datry, T., et al. (2022). Organizational principles of hyporheic exchange flow and biogeochemical cycling in river networks across scales. *Water Resources Research*, *58*(3), e2021WR029771. https://doi.org/10.1029/2021WR029771

Kruegler, J., Gomez-Velez, J., Lautz, L. K., & Endreny, T. A. (2020). Dynamic evapotranspiration alters hyporheic flow and residence times in the intrameander zone. *Water*, *12*(2), 424. https://doi.org/10.3390/w12020424

Larkin, R. G., & Sharp, J. M., Jr. (1992). On the relationship between river-basin geomorphology, aquifer hydraulics, and ground-water flow direction in alluvial aquifers. *Geological Society of America Bulletin*, *104*(12), 1608–1620. https://doi.org/10.1130/0016-7606(1992)104⟨1608:OTRBRB⟩2.3.CO;2

Lazarus, E. D., & Constantine, J. A. (2013). Generic theory for channel sinuosity. *Proceedings of the National Academy of Sciences*, *110*(21), 8447–8452. https://doi.org/10.1073/pnas.1214074110

19447973, 2024, 4, Downloaded from https://agupubs.onlinelibrary.wiley.com/doi/10.1029/2023WR036023, Wiley Online Library on [03/07/2024]. See the Terms and Conditions (https://onlinelibrary.wiley.com/terms-and-conditions) on Wiley Online Library for rules of use; OA articles are governed by the applicable Creative Commons License

Leopold, L. B., & Wolman, M. G. (1960). River meanders. *Geological Society of America Bulletin*, *71*(6), 769. https://doi.org/10.1130/0016-7606(1960)71[769:RM]2.0.CO;2

Lewandowski, J., Arnon, S., Banks, E., Batelaan, O., Betterle, A., Broecker, T., et al. (2019). Is the hyporheic zone relevant beyond the scientific community? *Water*, *11*(11), 2230. https://doi.org/10.3390/w11112230

Liao, L., Green, C. T., Bekins, B. A., & Böhlke, J. K. (2012). Factors controlling nitrate fluxes in groundwater in agricultural areas. *Water Resources Research*, *48*(6), W00L09. https://doi.org/10.1029/2011WR011008

Lindsey, B. D., Phillips, S. W., Donnelly, C. A., & Speiran, G. K. (2003). *Residence times and nitrate transport in ground water discharging to streams in the Chesapeake Bay Watershed*. US Geological Survey Water….

McClain, M. E., Boyer, E. W., Dent, C. L., Gergel, S. E., Grimm, N. B., Groffman, P. M., et al. (2003). Biogeochemical hot spots and hot moments at the interface of terrestrial and aquatic ecosystems. *Ecosystems*, *6*(4), 301–312. https://doi.org/10.1007/s10021-003-0161-9

McGuire, K., & McDonnell, J. (2006). A review and evaluation of catchment transit time modeling. *Journal of Hydrology*, *330*(3–4), 543–563. https://doi.org/10.1016/j.jhydrol.2006.04.020

Millington, R. J., & Quirk, J. P. (1961). Permeability of porous solids. *Transactions of the Faraday Society*, *57*(0), 1200–1207. https://doi.org/10.1039/TF9615701200

Molz, F. J., Widdowson, M. A., & Benefield, L. D. (1986). Simulation of microbial growth dynamics coupled to nutrient and oxygen transport in porous media. *Water Resources Research*, *22*(8), 1207–1216. https://doi.org/10.1029/WR022i008p01207

Montgomery, K. (1996). Sinuosity and fractal dimension of meandering rivers. *Area*, *28*, 491–500. Retrieved from http://www.jstor.org/stable/10.2307/20003734

Moore, R. B., McKay, L. D., Rea, A. H., Bondelid, T. R., Price, C. V., Dewald, T. G., & Johnston, C. M. (2019). *User's guide for the National Hydrography Dataset Plus (NHDPlus) high resolution*. (Open-File Report No. 2019-1096) (Series: Open-File Report). U.S. Geological Survey. https://doi.org/10.3133/ofr20191096

Oldham, C. E., Farrow, D. E., & Peiffer, S. (2013). A generalized Damköhler number for classifying material processing in hydrological systems. *Hydrology and Earth System Sciences*, *17*(3), 1133–1148. https://doi.org/10.5194/hess-17-1133-2013

Perez, G., Gomez-Velez, J. D., Chen, X., Scheibe, T., Chen, Y., & Bao, J. (2021). Identification of characteristic spatial scales to improve the performance of analytical spectral solutions to the groundwater flow equation. *Water Resources Research*, *57*(12), e2021WR031044. https://doi.org/10.1029/2021WR031044

Peterson, E. W., & Sickbert, T. B. (2006). Stream water bypass through a meander neck, laterally extending the hyporheic zone. *Hydrogeology Journal*, *14*(8), 1443–1451. https://doi.org/10.1007/s10040-006-0050-3

Poole, G. C., Stanford, J. A., Running, S. W., & Frissell, C. A. (2006). Multiscale geomorphic drivers of groundwater flow paths: Subsurface hydrologic dynamics and hyporheic habitat diversity. *Journal of the North American Benthological Society*, *25*(2), 288–303. https://doi.org/10.1899/0887-3593(2006)25[288:mgdogf]2.0.co;2

Pringle, C. M. (2001). Hydrologic connectivity and the management of biological reserves: A global perspective. *Ecological Applications*, *11*(4), 981–998. https://doi.org/10.1890/1051-0761(2001)011[0981:HCATMO]2.0.CO;2

Pringle, C. M. (2003). What is hydrologic connectivity and why is it ecologically important? *Hydrological Processes*, *17*(13), 2685–2689. https://doi.org/10.1002/hyp.5145

Revelli, R., Boano, F., Camporeale, C., & Ridolfi, L. (2008). Intra-meander hyporheic flow in alluvial rivers. *Water Resources Research*, *44*(12). https://doi.org/10.1029/2008WR007081

Robertson, W. D., & Cherry, J. A. (1995). In situ denitrification of septic-system nitrate using reactive porous media barriers: Field trials. *Groundwater*, *33*(1), 99–111. https://doi.org/10.1111/j.1745-6584.1995.tb00266.x

Sawyer, A. H. (2015). Enhanced removal of groundwater-borne nitrate in heterogeneous aquatic sediments. *Geophysical Research Letters*, *42*(2), 403–410. https://doi.org/10.1002/2014GL062234

Schmadel, N. M., Harvey, J. W., Alexander, R. B., Boyer, E. W., Schwarz, G. E., Gomez-Velez, J. D., et al. (2020). Low threshold for nitrogen concentration saturation in headwaters increases regional and coastal delivery. *Environmental Research Letters*, *15*(4), 044018. https://doi.org/10.1088/1748-9326/ab751b

Seminara, G. (2006). Meanders. *Journal of Fluid Mechanics*, *554*(1), 271–297. https://doi.org/10.1017/S0022112006008925

Seminara, G., Zolezzi, G., Tubino, M., & Zardi, D. (2001). Downstream and upstream influence in river meandering. Part 2. Planimetric development. *Journal of Fluid Mechanics*, *438*, 213–230. https://doi.org/10.1017/S0022112001004281

Smith, R. A., Alexander, R. B., & Schwarz, G. E. (2003). Natural background concentrations of nutrients in streams and rivers of the conterminous United States. *Environmental Science & Technology*, *37*(14), 3039–3047. https://doi.org/10.1021/es020663b

Snow, R. S. (1989). Fractal sinuosity of stream channels. *Pure and Applied Geophysics*, *131*(1), 99–109. https://doi.org/10.1007/bf00874482

Song, X., Chen, X., Zachara, J. M., Gomez-Velez, J. D., Shuai, P., Ren, H., & Hammond, G. E. (2020). River dynamics control transit time distributions and biogeochemical reactions in a dam-regulated river corridor. *Water Resources Research*, *56*(9), e2019WR026470. https://doi.org/10.1029/2019WR026470

Stelzer, R. S., & Bartsch, L. A. (2012). Nitrate removal in deep sediments of a nitrogen-rich river network: A test of a conceptual model. *Journal of Geophysical Research*, *117*(G2), G02027. https://doi.org/10.1029/2012JG001990

Stelzer, R. S., Scott, J. T., & Bartsch, L. A. (2015). Buried particulate organic carbon stimulates denitrification and nitrate retention in stream sediments at the groundwater–surface water interface. *Freshwater Science*, *34*(1), 161–171. https://doi.org/10.1086/678249

Sterle, G., Perdrial, J., Kincaid, D. W., Underwood, K. L., Rizzo, D. M., Haq, I. U., et al. (2024). CAMELS-Chem: Augmenting CAMELS (Catchment Attributes and Meteorology for Large-sample Studies) with atmospheric and stream water chemistry data. *Hydrology and Earth System Sciences*, *28*(3), 611–630. https://doi.org/10.5194/hess-28-611-2024

Stonedahl, S. H., Harvey, J. W., & Packman, A. I. (2013). Interactions between hyporheic flow produced by stream meanders, bars, and dunes. *Water Resources Research*, *49*(9), 5450–5461. https://doi.org/10.1002/wrcr.20400

Tonina, D., & Buffington, J. M. (2009). Hyporheic exchange in mountain rivers I: Mechanics and environmental effects: Mechanics of hyporheic exchange. *Geography Compass*, *3*(3), 1063–1086. https://doi.org/10.1111/j.1749-8198.2009.00226.x

Troch, P. A., Berne, A., Bogaart, P., Harman, C., Hilberts, A. G. J., Lyon, S. W., et al. (2013). The importance of hydraulic groundwater theory in catchment hydrology: The legacy of Wilfried Brutsaert and Jean-Yves Parlange. *Water Resources Research*, *49*(9), 5099–5116. https://doi.org/10.1002/wrcr.20407

Vermeulen, B., Hoitink, A. J. F., Zolezzi, G., Abad, J. D., & Aalto, R. (2016). Multiscale structure of meanders. *Geophysical Research Letters*, *43*(7), 3288–3297. https://doi.org/10.1002/2016GL068238

Vušanović, I., & Voller, V. R. (2021). Reduced complexity solidification models. *International Journal of Heat and Mass Transfer*, *169*, 120923. https://doi.org/10.1016/j.ijheatmasstransfer.2021.120923

19447973, 2024, 4, Downloaded from https://agupubs.onlinelibrary.wiley.com/doi/10.1029/2023WR036023, Wiley Online Library on [03/07/2024]. See the Terms and Conditions (https://onlinelibrary.wiley.com/terms-and-conditions) on Wiley Online Library for rules of use; OA articles are governed by the applicable Creative Commons License

Wang, C., Gomez-Velez, J. D., & Wilson, J. L. (2022). Dynamic coevolution of baseflow and multiscale groundwater flow system during prolonged droughts. *Journal of Hydrology*, *609*, 127657. https://doi.org/10.1016/j.jhydrol.2022.127657

Ward, A. S., & Packman, A. I. (2019). Advancing our predictive understanding of river corridor exchange. *WIREs Water*, *6*(1), e1327. https://doi.org/10.1002/wat2.1327

White, D. S., Elzinga, C. H., & Hendricks, S. P. (1987). Temperature patterns within the hyporheic zone of a northern Michigan River. *Journal of the North American Benthological Society*, *6*(2), 85–91. https://doi.org/10.2307/1467218

Wu, L., Gomez-Velez, J. D., Krause, S., Singh, T., Wörman, A., & Lewandowski, J. (2020). Impact of flow alteration and temperature variability on hyporheic exchange. *Water Resources Research*, *56*(3), e2019WR026225. https://doi.org/10.1029/2019WR026225

Wu, L., Gomez-Velez, J. D., Krause, S., Wörman, A., Singh, T., Nützmann, G., & Lewandowski, J. (2021). How daily groundwater table drawdown affects the diel rhythm of hyporheic exchange. *Hydrology and Earth System Sciences*, *25*(4), 1905–1921. https://doi.org/10.5194/hess-25-1905-2021

Zarnetske, J. P., Haggerty, R., Wondzell, S. M., & Baker, M. A. (2011a). Dynamics of nitrate production and removal as a function of residence time in the hyporheic zone. *Journal of Geophysical Research*, *116*(G1), G01025. https://doi.org/10.1029/2010JG001356

Zarnetske, J. P., Haggerty, R., Wondzell, S. M., & Baker, M. A. (2011b). Labile dissolved organic carbon supply limits hyporheic denitrification. *Journal of Geophysical Research*, *116*(G4), G04036. https://doi.org/10.1029/2011JG001730

Zarnetske, J. P., Haggerty, R., Wondzell, S. M., Bokil, V. A., & González-Pinzón, R. (2012). Coupled transport and reaction kinetics control the nitrate source-sink function of hyporheic zones. *Water Resources Research*, *48*(11), W11508. https://doi.org/10.1029/2012WR011894

Zheng, J., Thornton, P. E., Painter, S. L., Gu, B., Wullschleger, S. D., & Graham, D. E. (2019). Modeling anaerobic soil organic carbon decomposition in Arctic polygon tundra: Insights into soil geochemical influences on carbon mineralization. *Biogeosciences*, *16*(3), 663–680. https://doi.org/10.5194/bg-16-663-2019

Zheng, L., Cardenas, M. B., & Wang, L. (2016). Temperature effects on nitrogen cycling and nitrate removal-production efficiency in bed form-induced hyporheic zones. *Journal of Geophysical Research: Biogeosciences*, *121*(4), 2015JG003162. https://doi.org/10.1002/2015JG003162

Zhou, Y., Ritzi, R. W., Jr., Soltanian, M. R., & Dominic, D. F. (2014). The influence of streambed heterogeneity on hyporheic flow in gravelly rivers. *Groundwater*, *52*(2), 206–216. https://doi.org/10.1111/gwat.12048

19447973, 2024, 4, Downloaded from https://agupubs.onlinelibrary.wiley.com/doi/10.1029/2023WR036023, Wiley Online Library on [03/07/2024]. See the Terms and Conditions (https://onlinelibrary.wiley.com/terms-and-conditions) on Wiley Online Library for rules of use; OA articles are governed by the applicable Creative Commons License